JGR Planets

RESEARCH ARTICLE
10.1029/2019JE006218

Key Points:
- Compositions of outcrops of impact melt rock at the Haughton impact structure were determined quantitatively using imaging spectroscopy
- Impact melt rock in this sedimentary target is incompletely mixed and heterogeneous
- Clasts and groundmass in the melt rock are sourced from different depths in the target stratigraphy depending on location in the structure

Supporting Information:
- Supporting Information S1

Correspondence to:
R. N. Greenberger,
rgreenbe@caltech.edu

Citation:
Greenberger, R. N., Ehlmann, B. L., Osinski, G. R., Tornabene, L. L., & Green, R. O. (2020). Compositional heterogeneity of impact melt rocks at the Haughton impact structure, Canada: Implications for planetary processes and remote sensing. *Journal of Geophysical Research: Planets*, *125*, e2019JE006218. https://doi.org/10.1029/2019JE006218

Received 4 OCT 2019
Accepted 28 JUL 2020
Accepted article online 7 AUG 2020

Compositional Heterogeneity of Impact Melt Rocks at the Haughton Impact Structure, Canada: Implications for Planetary Processes and Remote Sensing

Rebecca N. Greenberger[1], Bethany L. Ehlmann[1,2], Gordon R. Osinski[3,4], Livio L. Tornabene[3,4,5], and Robert O. Green[2]

[1]Division of Geological and Planetary Sciences, California Institute of Technology, Pasadena, CA, USA, [2]Jet Propulsion Laboratory, California Institute of Technology, Pasadena, CA, USA, [3]Department of Earth Sciences, University of Western Ontario, London, Ontario, Canada, [4]Institute for Earth and Space Exploration, University of Western Ontario, London, Ontario, Canada, [5]SETI Institute, Mountain View, CA, USA

Abstract Connecting the surface expression of impact crater-related lithologies to planetary or regional subsurface compositions requires an understanding of material transport during crater formation. Here, we use imaging spectroscopy of six clast-rich impact melt rock outcrops within the well-preserved 23.5-Ma, 23-km diameter Haughton impact structure, Canada, to determine melt rock composition and spatial heterogeneity. We compare results from outcrop to outcrop, using clasts, groundmass, and integrated clast-groundmass compositions as tracers of transport during crater-fill melt rock formation and cooling. Supporting laboratory imaging spectroscopy analyses of 91 melt-bearing breccia and clast samples and microscopic X-ray fluorescence elemental mapping of cut samples paired with spectroscopy of identical surfaces validate outcrop-scale lithological determinations. Results show different clast-rich impact melt rock compositions at three sites kilometers apart and an inverse correlation between silica-rich (sandstone, gneiss, and phyllosilicate-rich shales) and gypsum-rich rocks that suggests differences in source depth with location. In the target stratigraphy, gypsum is primarily sourced from ~1-km depth, while gneiss is from >1.8-km depth, sandstone from >1.3 km, and shales from ~1.6–1.7 km. Observed heterogeneities likely result from different excavation depths coupled with rapid quenching of the melt due to high content of cool clasts. Results provide quantitative constraints for numerical models of impact structure formation and give new details on melt rock heterogeneity important in interpreting mission data and planning sample return of impactites, particularly for bodies with impacts into sedimentary and volatile-bearing targets, e.g., Mars and Ceres.

Plain Language Summary When extraterrestrial asteroids/comets over a certain size strike Earth's surface or other Solar System bodies, they form craters, and their energy brings buried rocks to the surface where we can study them. This process melts some rocks, which mix with unmelted rock and solidify to form a new rock type, impact melt rock. A key question is how much the melt rock's composition changes around the crater, which tells us if and how impact melt rocks preserve the nature of buried materials, which are otherwise unobservable. We used a portable imaging spectrometer instrument. Each pixel in the resulting image records visible and infrared light reflected off the rock. The way the rock absorbs light indicates the minerals present and how much of each is in the melt rock. We studied a crater in Canada by measuring large field outcrops and small lab samples. Across all spatial scales, we find large differences in impact melt rock composition with location in the crater, recording rocks excavated from different depths. These results improve our understanding of how craters form, provide percentage differences in composition that computational models of crater formation must reproduce, and help interpret similar rocks observed on Mars, Ceres, and elsewhere.

1. Introduction

1.1. Impact Cratering in the Solar System

Hypervelocity impacts are a geological process affecting every solid solar system body. Impacts modify surfaces and excavate subsurface lithologies that can then be studied by remote sensing and in situ measurements. In many cases, impact craters are the primary windows into subsurface lithologies of other

planetary bodies and permit identification of lithologies that might not otherwise be observable. For example, a study of fresh lunar highlands craters of different sizes found an upper crust dominated by norite, while the deeper crust excavated by larger craters contained less norite and more gabbro, anorthosite, and troctolite compositions (Pieters, 1986). Later work discovered excavated spinel within Moscoviense Basin (Pieters et al., 2011). A variety of primary and secondary minerals have been identified on Mars, including many associated with impact structures (e.g., Bibring et al., 2005; Ehlmann et al., 2009; Mustard et al., 2008; C. Pan et al., 2015; L. Pan et al., 2017; Sun & Milliken, 2015). The Mars Exploration Rover Opportunity landed in an impact crater and has explored others, investigating impacted sulfate-rich sedimentary rocks at the ~750-m diameter Victoria crater (Squyres et al., 2009) and melt and older crustal rocks excavated at the larger, ~22-km diameter Endeavour crater (Arvidson et al., 2014; Squyres et al., 2012). An understanding of how impactites represent and sample subsurface lithologies is critical to proper interpretation of crater-related compositional units.

Melt is an important byproduct of meteorite impacts across the solar system and is present in all but the smallest craters (e.g., Dence, 1971; Grieve et al., 1977; Grieve & Cintala, 1997; Osinski et al., 2018). It forms through melting of target rocks during hypervelocity impacts and contains clasts of variably shocked target rock that can react with and, in some cases, are assimilated by the melt (e.g., Dressler & Reimold, 2001; Grieve, 1987). Layers and discrete lenses of impact melt are present on the floors of fresh impact structures, making them a spatially important impactite viewed from nadir remote sensing observations. The composition of the melt and clasts, which are derived from throughout the target stratigraphy, provides key information about the presence and variety of compositional subsurface units.

1.2. Impact Melt Heterogeneity

Some studies of terrestrial impact structures have suggested that impact melt sheets are largely homogenous chemically, with minor textural variations attributed to settling of clasts, differences in cooling rate, local reaction with or resorption of clasts, or hydrothermal alteration (e.g., Dressler & Reimold, 2001; Floran et al., 1976, 1978; Grieve, 1975; Grieve et al., 1977; Koeberl et al., 2012; Palme et al., 1979). It has at times been assumed that a compositionally diverse target will still produce homogenous melt sheets (Palme et al., 1979; Ryder & Wood, 1977), and, indeed, the observation of melt sheet homogeneity, and specifically the presence of neighboring clasts within the impact melt from disparate locations pre-impact, was suggested as a constraint for models of impact crater formation that must provide a mechanism for extensive mixing (Grieve et al., 1977). Simonds and Kieffer (1993) suggest "intense mixing during emplacement" of impact melt at the Manicouagan structure and for melt sheets in general, and O'Connell-Cooper and Spray (2011) describe isotopic homogenization of the Manicouagan melt rock. Similarities in major element composition of impact glasses from the Popigai structure have also been proposed as evidence for homogenization of impact melt (Raikhlin & Masaitis, 2019). Remote sensing and modeling studies often implicitly or explicitly consider the impact melt as single unit, mapping a single "impact melt" unit or discussing the composition of "impact melt." Petrologic and other modeling studies have also assumed homogenous impact melt as a starting point (e.g., Cassanelli & Head, 2016; Vaughan et al., 2013) and have suggested that formation and mixing of impact melt homogenizes the lunar crust (Cassanelli & Head, 2016).

Within some of the field studies referenced in the previous paragraph, local mafic melts at the Manicouagan structure (Floran et al., 1976, 1978) and small variations in melt composition at Mistastin (Grieve, 1975) were suggested to result from incomplete mixing or differential assimilation of clasts. Further work at Mistastin documented heterogeneity of impact melt rocks at microscopic scales and between outcrops (Marion & Sylvester, 2010). Dressler and Reimold (2001) described a variety of examples of melt heterogeneity, though they suggest that impact melts are dominantly homogenous. At the Haughton structure, variations in the proportions of limestone clasts and the presence of gypsum only near uplifted gypsum-bearing lithologies have been noted qualitatively (Redeker & Stöffler, 1988), and considerable heterogeneities were documented by Osinski, Spray, and Lee (2005). Systematic heterogeneities observed by Osinski et al. (2008) have been tied to heterogeneous sedimentary target rocks. Analyses of sampled clasts at the Ries structure show spatial differences in clast lithologies, though several of the sampled outcrops are located outside of the crater rim and therefore would be more difficult to physically mix with melt-bearing crater fill (Siegert & Hecht, 2018; von Engelhardt, 1997). Evidence of heterogeneous melt rock is not unique to Earth. While earlier remote sensing spectral observations of the lunar surface at 100s of m- to km-scale resolution tended to favor the view of

Figure 1. Photos of clast-rich impact melt rock at the Haughton impact structure described by Osinski and Spray (2001, 2003). The presence of large clasts and blocks prohibits a study of impact melt rock heterogeneity at the scale of outcrops through traditional field methods and requires novel measurement techniques, such as imaging spectroscopy.

homogenous melt units in association with impact craters such as Kepler or Copernicus (e.g., Pinet et al., 1993; Öhman et al., 2014), recent spectral and radar observations suggest more heterogeneity, with various degrees of incomplete mixing (e.g., Dhingra et al., 2013; Neish et al., 2014).

1.3. Approach and Objectives

A quantitative assessment of the heterogeneity of impact melt rocks at the scale of outcrops observable from orbital and landed planetary missions has not yet been performed. Using traditional geologic field methods, a study of this type is difficult, if not impossible, because of the sheer number of clasts, variable clast size, and variable clast content (Figure 1). There is no hand sample that can be collected with each lithology present in the proportions of the outcrop and thus representative of the outcrop. Siegert and Hecht (2018) aggregated compositions of thousands of clasts from the Ries structure previously analyzed by von Engelhardt (1997) and Schmitt et al. (2017) and found compositional heterogeneities in suevite, but the abundances of each lithology by location differ for each of the two previous studies (see Tab. 6 of Siegert & Hecht, 2018). To address this challenge of outcrop scale mapping of heterogeneity, we used imaging spectroscopy of impact

melt rock outcrops at the Haughton impact structure, Canada, to quantitatively map the compositional heterogeneity of full outcrops of impact melt in the field and their associated clasts and groundmass in the lab.

Imaging spectroscopy was initially developed for airborne and orbital platforms (Goetz et al., 1985), and imaging spectroscopy of outcrops in the field is an emerging technique for geological applications (e.g., Greenberger et al., 2015). Imaging spectroscopy of melt rock outcrops permits determination of the composition of entire heterogeneous outcrops by measuring reflected light at many contiguous wavelengths to provide a spectrum (Goetz et al., 1985), which can be analyzed to determine mineralogy for every pixel within an image. Comparing the bulk compositions of multiple outcrops within a single impact structure provides insights into the presence or absence of large-scale mixing during melt rock formation and emplacement. The null hypothesis is that, if impact melt is well-mixed and homogenized, the groundmass material as well as the clasts within the melt rock should be compositionally homogenized between outcrops. On the other hand, poorly mixed melt rock would exhibit outcrop-to-outcrop variations.

Here, we describe the results from quantitative mapping of impact melt rock composition at multiple scales, relating observed heterogeneities within the Haughton structure to target rock subsurface stratigraphy. The results of this study have implications for our understanding of melt formation, homogenization, and emplacement processes during meteorite impacts as well as interpretations of lithologies within impact melt units in planetary studies.

2. Geological Setting

The Haughton impact structure (Figure 2) is located at 75°22′N, 89°41′W, on Devon Island, Nunavut, Canada (Frisch & Thorsteinsson, 1978). This complex structure has an apparent diameter of ~23 km (Osinski, Lee, Spray et al., 2005) and is 23.5 ± 2.0 Ma (Young et al., 2013). The target stratigraphy is well characterized, with ~1,880 m of Lower Paleozoic sedimentary strata overlying the crystalline basement, which is mostly gneiss with limited granitic plutonic rocks and dolerite dikes (Figure 2; Osinski, Lee, Spray et al., 2005). The volumetrically dominant crater-fill unit is the impact melt rock, which consists of a silicate-carbonate-anhydrite groundmass of melt exhibiting liquid immiscibility textures with abundant clasts of sedimentary (limestone, dolomite, sandstone, shale, and evaporite) and basement rocks (gneiss, granite, and dolerite) (Osinski, Lee, Spray et al., 2005; Osinski, Spray, & Lee, 2005; Osinski & Spray, 2001, 2003). According to the modified classification scheme of Osinski et al. (2008), this unit is clast-rich impact melt rock. The melt unit currently covers ~54 km^2 with a thickness of up to 125 m and is estimated to have originally covered 115 km^2 with a thickness of more than 200 m (Osinski, Lee, Spray et al., 2005). The melt rock has been well-characterized by field description and electron microprobe-scale chemical composition by Osinski, Lee, Spray et al. (2005), Osinski, Spray, and Lee (2005), and Osinski and Spray (2001, 2003), but those studies did not map the composition of or quantify the clasts within the large melt rock outcrops due to the aforementioned challenges of doing so with traditional field geology methods.

The Haughton structure was selected for this imaging spectroscopy investigation of the melt rock based on its exceptional preservation state, resulting from the dominantly cold and arid environmental conditions since its formation, lack of vegetation, lichen, and moss (Figure 1), and outcrop accessibility (Osinski, Lee, Spray et al., 2005). The well-characterized and nearly flat-lying target stratigraphy permit interpretations of the source depths of clasts found within the melt rock (Figure 2) (Osinski, Lee, Spray et al., 2005; Osinski, Spray, & Lee, 2005). This study would be challenging in large terrestrial impact structures at more temperate latitudes due to weathering and formation of coatings, rinds, and varnish on the rock and increased ground cover (e.g., soil and vegetation). While erosion has removed some Haughton melt rock material, outcrops of pristine impact melt rock have recently been exposed via erosion by streams with minimal weathering since exposure. Orbital remote sensing shows the Haughton crater fill at a broad scale as a characteristically light-toned unit most consistent spectrally with a mix of the dominant target lithologies (i.e., carbonates, gypsum and a silica-bearing component) (Tornabene et al., 2005). While impact-generated hydrothermal alteration has been documented at Haughton, it tends to be structurally controlled and, within the melt rock, occurs as isolated small vugs and veins easily distinguished morphologically from the unaltered melt rock (Osinski et al., 2001; Osinski, Lee, Parnell et al., 2005). This is in contrast to structures such as the Ries, where hydrothermal alteration and later low-temperature weathering have pervasively altered the melt-bearing suevite (e.g., Muttik et al., 2008, 2010; Newsom et al., 1986;

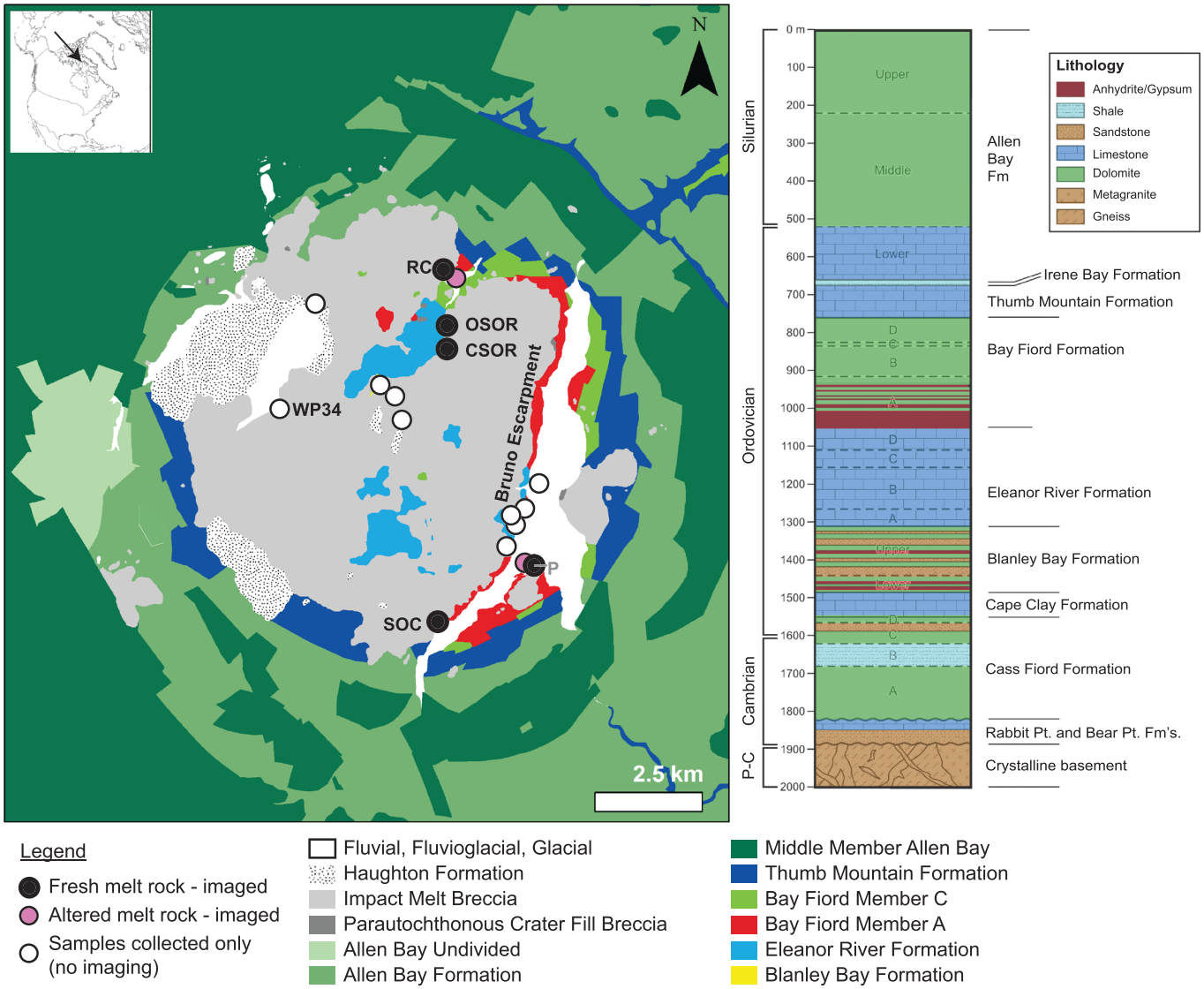

Figure 2. Geologic map of the Haughton impact structure and target rock stratigraphy (modified from Osinski, Lee, Spray et al., 2005) with colors indicative of bulk composition as would be determined via spectroscopy (red = gypsum; greens = dolomite; blues = calcite; brown = Si-OH; gray = mixed Si-OH and carbonate; cyan (strat column only) = illite; yellow = dolomite, Si-OH, and gypsum). These colors are similar to the compositional color scheme of subsequent figures. Fluvial, fluvioglacial, and glacial sediments and the Haughton Formation (post-impact lacustrine sediments) are not part of the target rock and are not colored on the map based on composition. Key imaging and sampling locations are labeled. P = Pinnacle. RC = Rhinoceros Creek. SOC = South of Camp. OSOR = Overhang South of Rhinoceros Creek. CSOR = Creek south of Rhinoceros Creek. WP34 = Waypoint 34 (westernmost outcrop). See Table 1 for descriptions and coordinates of outcrops. Samples were collected at all outcrops that were imaged.

Osinski, 2005). All of these characteristics make Haughton a unique site to investigate well-preserved, little-altered melt rock using ground-based imaging spectroscopy.

Compositional mapping from orbital multispectral data sets at 15–60 m/pixel mapped the regional stratigraphy, crater fill, and uplift within the impact structure (Tornabene et al., 2005) but did not provide definitive mineralogies, distinguish individual clasts, nor observe the near vertical exposures of pristine melt rock. A previous imaging spectroscopy study at the Haughton structure (Greenberger et al., 2016) characterized a hydrothermal calcite-marcasite vug and its weathering products using a more limited wavelength range but did not image or discuss the unaltered melt rock that is the focus of this paper. Carbonate samples from Haughton were measured with point spectroscopy of bulk rock samples and powders in the laboratory for a study of carbonate detection with implications for Mars (Cloutis et al., 2010).

Table 1
Details of Outcrops Measured in the Field for This Study with an Imaging Spectrometer

Date and time (all 2016)	Latitude	Longitude	Name	Description	Sky conditions	Distance to outcrop
22 July (14:55–15:45) 24 July (12:35, 16:00) 27 July (21:00) 28 July (13:50–15:00)[a]	75.415°N	89.635°W	Rhinoceros Creek (RC)	Freshly exposed clast-rich impact melt rock outcrop along Rhinoceros Creek	22 July: cloudy/part sun; 27 July: variable clouds; 28 July: mostly sunny	20–70 m
25 July (1:45) 6 August (10:10)[a]	75.353°N	89.549°W	Pinnacle (P)	Pinnacle of clast-rich impact melt rock exposed atop larger scree slope	25 July: mostly cloudy; 6 August: full sun	10–20 m
28 July (00:25)	75.402°N	89.630°W	Overhang South of Rhinoceros Creek (OSOR)	Clast-rich impact melt rock exposed where rock was undercut along gully	Cloud partly blocking sun; near midnight	5 m
27 July (22:30–23:20)	75.397°N	89.633°W	Creek South of Rhinoceros Creek (CSOR)	Couple meters of clast-rich impact melt rock exposed along creek in central region of crater	1 cloud in the sky tracking with sun; near midnight	5–8 m
31 July (11:20–11:25)[a]	75.374°N	89.532°W	Bruno Escarpment	Eroded melt rock and gullies of Bruno Escarpment, within view of Haughton River Valley camp	Large break in otherwise cloudy sky	0.5–3 km
4 August (13:20) 6 August (11:30–11:45)[a]	75.340°N	89.627°W	South of Camp (SOC)	Clast-rich impact melt rock cut by gullies in southern portion of crater	4 August: Cloudy and snowing, occasional breaks in clouds; 6 August: Full sun	8–20 m

[a]Best quality acquisitions used for this paper.

The methods and instruments used for field measurements in this paper differ from Tornabene et al. (2005) and Cloutis et al. (2010) and significantly expand on that of Greenberger et al. (2016) and therefore are described in full in section 3.

3. Methods

3.1. Sampling and Imaging Strategy

Five outcrops of pristine melt rock were imaged around the Haughton structure during the July–August 2016 field season (Figure 2; Table 1). Generally, outcrops were selected for best exposure of melt rock, distribution within the structure, and access. Images should ideally be acquired under clear skies to maximize the solar radiation incident on the outcrop while minimizing atmospheric attenuation that must later be corrected. Since cloudless skies were few this particular field season, images unfortunately also needed to be acquired for this study in moments of sun between patchy clouds. While images of more outcrops would have been ideal, we were limited by an uncharacteristically rainy and snowy summer field season that precluded imaging much of the time. (We note that unreliable weather would not be a factor for application of this technique to impact craters on most other bodies in the solar system. Airless bodies such as the Moon or Ceres would have no atmospheric attenuation and would be similar to laboratory measurements. Mars' atmosphere is much thinner than Earth's, meaning that there is relatively little attenuation of incoming solar radiation, outside of periods with large dust storms. We would not recommend the visible-shortwave infrared (VSWIR) wavelength range on Venus or Titan). In addition to pristine outcrops, we acquired one additional image of 2+ km of Bruno Escarpment during a ~15-min break in the clouds. The escarpment is heavily weathered and covered with soil crusts and broken pieces of the melt rock, but this image provides an additional data point under the assumption that melt rock of uniform composition weathered under the same conditions should yield the same mineralogies, whereas heterogeneous compositions of melt rock should weather to different compositions reflecting differences in the primary melt rock.

Two types of samples were collected from outcrops: individual clasts of single lithologies and polymict, clast-rich impact melt rock breccias. The single lithology clasts were selected during careful examination of the outcrop and scree to capture the variety of lithologies identified visually within outcrops and later analyze the samples to confirm detections of those lithologies with imaging methods. The breccias were sampled from diverse, spatially separated locations on the outcrop that visually had a variety of clasts separated by groundmass (as opposed to large clasts or blocks) and were also collected from scree slopes at the base of

outcrops. The breccia samples permit validation of our lithologic mapping techniques and sample-to-sample and sample-to-outcrop comparisons. Calibration targets with three or four different materials of known spectral properties were placed in each scene and also provided points of calibration and validation.

3.2. Imaging Spectroscopy

We used the Caltech visible-shortwave infrared (VSWIR) imaging spectrometer system, which was custom built by Headwall Photonics, Inc. This instrument contains two 16-bit, f/2.5 aperture sensors and measures light collected through a vertical slit. A complementary metal-oxide semiconductor (CMOS) sensor covers visible-near infrared (VNIR; 0.4–1.0 μm) wavelengths, and a Stirling-cooled Mercury Cadmium Telluride (MCT) sensor samples shortwave infrared (SWIR; 0.90–2.60 μm) wavelengths. The VNIR sensor has 1,600 spatial elements × 372 spectral elements with 5-nm Full-Width Half-Maximum (FWHM) spectral resolution and a spectral sampling interval of 1.625 nm. The SWIR sensor has 640 spatial elements × 285 spectral bands with 6-nm FWHM spectral resolution. The two sensors are co-boresighted on an optical bench with a dichroic beam splitter. Angular fields of view are 25.4° (VNIR) and 30.3° (SWIR), giving pixel sizes in the SWIR of a few cm/pixel in the field at distances of 10s of meters from outcrops and 200–250 μm/pixel at ~20-cm standoff in the laboratory. VNIR spatial resolution is ~3× higher than SWIR. While data were acquired from both sensors, our analyses focus on SWIR data, which were most effective for compositional discrimination of clasts of the particular lithologies present at this site.

Images of outcrops were acquired with this system mounted on a rotational stage atop a tripod. The instrument is a pushbroom-type imaging spectrometer, meaning that image cubes were built by acquiring vertical lines of data while the stage rotated, with frame periods selected for both VNIR and SWIR sensors to match the rotational stage speed such that the angular horizontal distance covered by each pixel in a single frame was the same as that sampled vertically. Labsphere reference panels were placed in each scene to assist in calibration to reflectance. For images acquired close enough to outcrops to resolve smaller targets, a single ~25-cm square multi-reflectance Spectralon contrast target was used that contained four strips of material of ~12%, 25%, 50%, and 99% reflectance. For distances to outcrops at which those individual strips could not be resolved, three Labsphere panels were used with reflectance values of ~5%, 20%, and 99%. All panels have calibration files with spectra that are traceable to the U.S. National Institute of Standards and Technology.

Samples collected from the field were imaged in the laboratory with the imaging spectrometer mounted vertically, looking downward at a horizontal translational stage, which moved samples at a controlled, constant speed below the imaging spectrometer slit to build an image cube. Samples were illuminated with a halogen slit lamp, and images were acquired relative to a 99% Spectralon target.

3.3. Image Calibration and Processing Methods

Step 1: Process the data from raw detector counts in Digital Number (DN) to reflectance (Figure 3, Step 1)

Laboratory data were corrected pixel by pixel by subtracting a dark current measurement and dividing by an image of Spectralon at approximately the same height as the sample face with the same illumination. This corrects for both spatial nonuniformities on the sensor and differences in illumination across the sample. Images were then corrected for the non-Lambertian spectral properties of Spectralon by multiplying by its true reflectance.

Field data were corrected for instrumental effects by first subtracting a dark current measurement acquired with the lens cap on (the SWIR sensor has a shutter, while the VNIR does not) and then doing a multiplicative flat field correction derived from laboratory integrating sphere measurements to remove spatial nonuniformities. Next, the darkest pixels in the scene were located by stretching the image display contrast, and the resulting mean spectrum was subtracted from every pixel. This correction removes the additive effects of atmospheric scattering (Chavez Jr., 1996, 1988; Vincent, 1972). Finally, the entire scene was divided by the average spectrum of the in-scene 99% Spectralon panel and multiplicatively corrected for the reflectance properties of Spectralon. This step removes multiplicative atmospheric effects and corrects the scene to reflectance. Reflectance images were smoothed using a 3 × 3 × 3 (spatial x/spatial y/spectral) boxcar average to reduce noise and striping.

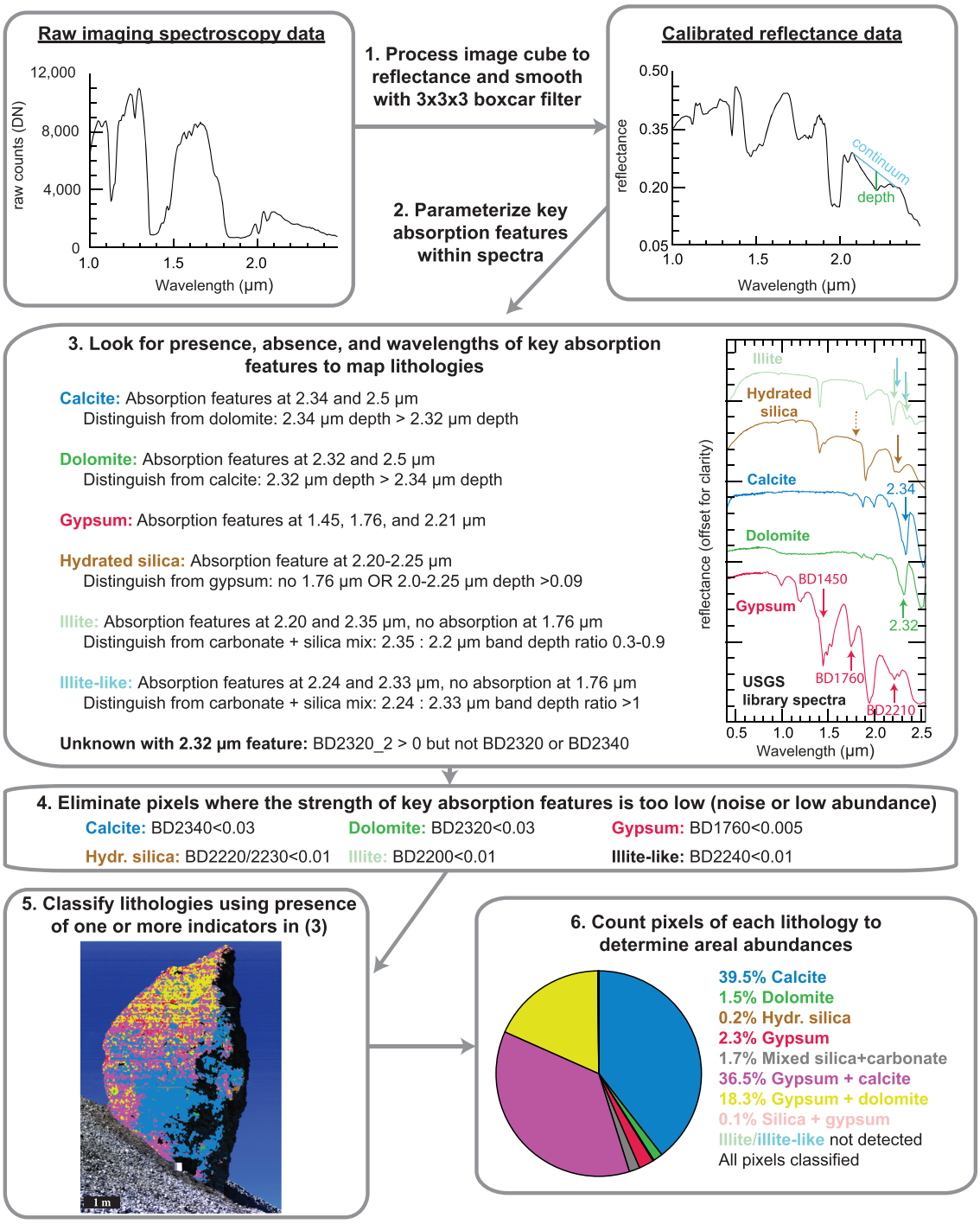

Figure 3. Workflow showing data processing steps from the raw detector counts of the instrument to lithologic mapping of the outcrop or samples and quantification of areal abundances of each lithology. See Tables 2–4 for full formulas used for classification. In Step 3, an example of the features measured by the band depth (BD) parameters is shown for gypsum and corresponds with Table 2 and 3, although there are multiple formulations of some parameters, for example "BD1760" includes BD1760_field, BD1760_field2, and BD1760_narrow_field (similar or same center wavelength, different continuum points).

Illumination geometry varies across the scene as the imaging spectrometer rotates and facets of the outcrop have different orientations. Correction to absolute reflectance for the geometry of observations would require lidar or stereo-analysis of the outcrop to account for orientation of every pixel of the outcrop, and these data were not available. The standard correction for illumination geometry is a multiplicative cosine

factor, assuming isotropic scattering, applied to all wavelengths (Hapke, 1981). Because our subsequent mineral mapping methods are all multiplicative and operate on single pixels, that cosine factor is canceled out in the calculations, and our mineral mapping methods are independent of illumination geometry.

Step 2: Parameterize single spectral absorption features

Spectral parameters (Figure 3, Step 2) were calculated, mapping the depths of absorption bands, slopes, and other key features characteristic of specific mineral phases (e.g., Clark & Roush, 1984; Pelkey et al., 2007; Viviano-Beck et al., 2014). Formulas are given in Table 2 and were implemented with IDL scripts that operated pixelwise on the scene.

Step 3: Map minerals through combinations of parameterized absorption features

Mineral indicators were calculated by searching for the presence and absence of characteristic combinations of parameters from Step 2 indicative of different minerals (Figure 3, Step 3; Table 3). These utilized combinations of key absorption features of different minerals reported in the literature and through analysis of library spectra of pure mineral specimens from the USGS spectral library (Clark et al., 2007; Kokaly et al., 2017). Automated analyses were conducted using the formulas in Table 3 implemented in IDL. Some mineral indicators check for the presence of a single absorption feature, calculated using more than one set of center and continuum wavelengths due to mixtures with other minerals affecting the continuum and/or to reduce noise in the final product. There are also comparisons and thresholds in cases where multiple minerals have similar or overlapping absorption features (see distinguishing criteria in Figure 3, Step 3). This strategy using combinations of absorption features was selected over algorithms such as linear unmixing (Adams et al., 1986, 1995) or Tetracorder (Clark et al., 2003) because the shocking of minerals within the target rock leads to broadening and other changes to absorption features within the spectra. Nevertheless, diagnostic overtone and combination bands of phyllosilicates remain visible after high shock pressures (Friedlander et al., 2015, 2016). Carbonates exhibit some peak broadening in X-ray diffraction data (Flemming et al., 2018; Skála, 2002; Skála & Jakes, 1999) but show little change in SWIR spectra (L. Pan et al., 2018).

Step 4: Eliminate mineral indicators at very low abundance (pixel by pixel)

Depths of absorption features depend primarily on abundance but are also influenced by texture. Because the goal of this study is to quantify lithologies, we choose to eliminate mineral indicators within pixels with depths of a key absorption feature less than a threshold (Figure 3, Step 4; Table 3), suggesting either that the mineral is of low relative abundance or the detection is noise. In either case, the mineral contributes little to the overall bulk composition of the outcrop. These thresholds were set to be ~5–10% of the maximum value of that absorption feature within all of the images and library spectra analyzed.

Step 5: Classify lithologies

Using the presence of one or more mineral indicators, pixels were assigned to the 11 spectral classes that comprised distinct compositional lithologies or mixtures (Figure 3, Step 5; Figure 4; Table 4; section 4.1). Pixels that did not meet the criteria for any of these spectral classes were grouped into a twelfth "unclassified" category, permitting us to iteratively refine the thresholds to classify more pixels within the scene and improve the mapping algorithms while also reducing the likelihood of a pixel being forced into an inappropriate classification. Some of the unclassified pixels are simply spectrally flat, as is the case for the mineral quartz. Others have weak spectral features not present above the level of noise in the image or are a rare lithology not represented by classifications above.

While we would ideally derive abundances of each mineral within each pixel, this is challenging at Haughton, and we retain lithologies that are mixtures of multiple compositions as distinct mixed lithology classes. As mentioned in Step 3, the shock process can broaden or change the spectra of different minerals. While the minerals observed at Haughton are generally still recognizable when shocked (Friedlander et al., 2015, 2016; L. Pan et al., 2018), determining endmember spectra to use in calculations of mineral abundances is difficult to impossible due to variations in shock level within hand samples and outcrops. Another challenge in selecting endmembers is that hydration levels of the silicate glass of the melt and within shocked quartz in clasts differ, changing the nature and depth of the Si-OH spectral absorption feature (e.g., Aines & Rossman, 1984; Anderson & Wickersheim, 1964; Goryniuk et al., 2004). In addition, these mixed lithologies are critical in understanding variations in the composition of the groundmass (section 5.1.2).

Table 2
Formulas for Each Parameter Used in Compositional Mapping

Parameter	Center wavelength, R (μm)	Continuum endpoints (μm)	Number of averages (center/left/right)	Band assignment	Reference(s)
R1440/R1490[a]	Reflectance at 1.440 / 1.490		1/1	OH-stretching overtones in sulfates; distinguish copiapite/fibroferrite from gypsum	Cloutis et al. (2006) and Greenberger et al. (2016)
BD1450_broad	1.45	1.31, 1.67	5/3/3	OH stretching overtone; highlights broad bands in minerals such as gypsum	Clark et al. (1990) and Greenberger et al. (2016)
BD1760_field	1.76	1.665, 2.106	3/3/3	Common in sulfates; OH/H_2O combination	Hunt et al. (1971) and Crowley et al. (2003) and Cloutis et al. (2006)
BD1760_field2	1.76	1.69, 2.17	3/3/3	See BD1760_field	
BD1760_narrow_field	1.751	1.727, 1.775	3/3/3	See BD1760_field	
BD2200_illite	2.20	2.15, 2.27	3/3/3	Al-OH in phyllosilicates; also Si-OH	Aines and Rossman (1984), Anderson and Wickersheim (1964), and Clark et al. (1990)
BD2200_illite2	2.21	2.15, 2.285	3/3/3	See BD2200_illite2	
BD2200_2	2.20	2.16, 2.245	3/3/3	Si-OH, also Al-OH	Aines and Rossman (1984), Anderson and Wickersheim (1964), Clark et al. (1990)
BD2210	2.217	2.185, 2.245	3/3/3	S-Obending overtone in gypsum; may also map Al-OH and Si-OH	Cloutis et al. (2006)
BD2220_2	2.22	2.18, 2.25	3/3/3	Si-OH	Aines and Rossman (1984) and Anderson and Wickersheim (1964)
BD2220_3	2.22	2.184, 2.27	3/3/3	Si-OH	Aines and Rossman (1984) and Anderson and Wickersheim (1964)
BD2230	2.23	2.15, 2.27	3/3/3	Si-OH	Aines and Rossman (1984) and Anderson and Wickersheim (1964)
BD2240_illite	2.24	2.165, 2.275	3/3/3	AlMg-OH in phyllosilicates; also maps Si-OH	Clark et al. (1990)
BD2300_carb	2.30	2.16, 2.34	3/3/3	C-O overtone in carbonate; also maps Fe/Mg-OH in some phyllosilicates	Hunt and Salisbury (1971), Gaffey (1985, 1986, 1987), and Clark et al. (1990)
BD2320	2.318	2.12, 2.37	3/3/3	C-O overtone in carbonate; also maps Mg-OH in some phyllosilicates	Hunt and Salisbury (1971), Gaffey (1985, 1986, 1987), and Clark et al. (1990)
BD2320_2	2.322	2.29, 2.358	3/3/1	Unknown phase distinct from carbonate; assignment unknown but may be Mg-OH?	Clark et al. (1990)
BD2330_illite	2.33	2.165, 2.275	5/3/3	Fe/Mg-OH in phyllosilicates	Clark et al. (1990) and Bishop et al. (2008)
BD2330_illite2	2.33	2.275, 2.365	5/3/3	Fe/Mg-OH in phyllosilicates	Clark et al. (1990) and Bishop et al. (2008)
BD2340	2.34	2.18, 2.39	3/3/3	C-O overtone in carbonate; also maps Fe/Mg-OH in some phyllosilicates	Hunt and Salisbury (1971), Gaffey (1985, 1986, 1987), and Clark et al. (1990)
BD2340_narrow	2.34	2.286, 2.352	3/3/3	C-O overtone in carbonate; also maps Fe/Mg-OH in some phyllosilicates	Hunt and Salisbury (1971), Gaffey (1985, 1986, 1987), and Clark et al. (1990)
BD2340_compare	2.34	2.12, 2.37	3/3/3	C-O overtone in carbonate with same continuum as BD2320 to distinguish calcite and dolomite; also maps Fe/Mg-OH in some phyllosilicates	Hunt and Salisbury (1971), Gaffey (1985, 1986, 1987), and Clark et al. (1990)
BD2350_illite	2.35	2.15, 2.27	3/3/3	Fe/Mg-OH in phyllosilicates	Clark et al. (1990) and Bishop et al. (2008)
BD2350_illite2	2.35	2.15, 2.285	3/3/3	Fe/Mg-OH in phyllosilicates	Clark et al. (1990) and Bishop et al. (2008)
D2500[b]	2.47	2.40	3/3	C-O combination band in carbonates	Hunt and Salisbury (1971)

Note. BD = band depth calculated with the formula $1 - (R/R_c)$, where R is the reflectance at the center wavelength and R_c is the reflectance of a linear continuum at that wavelength (Clark & Roush, 1984). The endpoints of the continuum range used to calculate R_c are given.
[a]Ratio of reflectance values at two wavelengths. [b]Depth of downturn at 2.5 μm calculated as $1 - R2.47/R2.40$, where R is the reflectance at those wavelengths.

Table 3
Calculation of Mineral Indicators and Threshold Values for Positive Detections

Mineral	Chemical formula	Calculation[a]	Threshold value
Calcite	$CaCO_3$	BD2340 > 0.005, max (BD2340, BD2340_narrow, BD2340_compare) > BD2320, D2500 > 0, BD2300_carb<BD2340, BD2320_2 > 0.005	BD2340 > 0.03
Dolomite	$CaMg(CO_3)_2$	BD2320 > 0.005, max (BD2340, BD2340_narrow, BD2340_compare) < BD2320, D2500 > 0, BD2300_carb<BD2320, BD2320_2 > 0.005	BD2320 > 0.03
Gypsum	$CaSO_4 \cdot 2H_2O$	BD2210 > 0, (BD1760_field or BD1760_field2) > 0, BD1450_broad > 0, BD1760_narrow_field>0	(Max of BD1760_narrow_field, BD1760_field2) > 0.005
Hydrated silica 1	$SiO_2 \cdot nH_2O$	BD2200_2 > 0.005, BD2210 > 0.005, max (BD2220_2, BD2220_3) > 0.005	(Max of BD2220_2, BD2230) > 0.01
Hydrated silica 2	$SiO_2 \cdot nH_2O$	BD2230 > 0.005, BD2240_illite>0.005, max (BD2220_2, BD2220_3) > 0.005	(Max of BD2220_2, BD2230) > 0.01
Illite	$(K,H_3O)(Al,Mg,Fe)_2(Si,Al)_4O_{10}[(OH)_2,(H_2O)]$	max (BD2350_illite, BD2350_illite2) > 0.005, max (BD2200_illite, BD2200_illite2) > 0.005, 0.3 < max (BD2350_illite, BD2350_illite2)/max (BD2200_illite, BD2200_illite2) < 0.9, max (BD1760_field, BD1760_field2, BD1760_narrow_field) < 0.005	(Max of BD2200_illite, BD2200_illite2) > 0.01
Illite-like	Unknown, but likely similar to illite	BD2240_illite>0.005, max (BD2330_illite, BD2330_illite2) > 0.005, max (BD1760_field, BD1760_field2, BD1760_narrow_field) < 0.005, BD2240_illite/BD2330_illite>0.35	BD2240_illite>0.01
Unknown with 2.32-μm absorption	Unknown	BD2320_2 > 0, BD2320 < 0, BD2340 < 0	BD2320_2 > 0.005

[a]BD# refers to the band depths and spectral parameters given in Table 2.

Step 6: Compute areal abundances

Areal abundances of each lithology from Step 5 were determined by counting the number of pixels in each category and dividing by the total number of pixels in the outcrop. Spatially coherent lithologies, even if only a small portion of the image, are detections with high confidence, and we therefore report abundances with precisions of 0.1%. Outcrops were manually outlined to exclude sky, soil, and calibration targets in the abundance calculation.

Overall, this procedure produces accurate lithological abundance estimations, validated via hand sample comparison to independent data sets (see sections 3.4 and 4.4). Errors may result from coatings or nonlinear (intimate) spectral mixing obscuring certain components and the spatial resolution limiting the detection of minor lithologies within certain pixels. Our mixed lithology classes were developed to deal with overlapping absorption features making certain minerals difficult to distinguish when mixed, and the "unclassified" class may include minerals that are mostly featureless at these wavelengths (e.g., unweathered quartz or feldspars).

3.4. XRF Mapping

Microscopic X-ray fluorescence (XRF) mapping was selected to validate spectral interpretations of mineralogy due to XRF's ability to rapidly measure the chemical composition at a spatial resolution comparable to imaging spectroscopy over larger areas than typical microbeam analyses allow. While X-ray diffraction is a more common method of identifying mineralogy, distortion of primary mineral structures and the presence of amorphous glass and shocked materials due to the impact event mean that chemical composition is a better tracer of lithology in this instance. Importantly, XRF mapping also preserves spatial context for direct comparison.

Five of the hand samples of melt rock that were imaged in their bulk form were cut with a rock saw, sonicated in water to remove dust and loose material, and dried in an oven at 60°C. The resulting slices were analyzed with a Horiba Scientific XGT-7200 X-ray Analytical Microscope at the Los Angeles Natural History Museum to produce elemental maps. The analyses used a 50-μm beam, 30 kV X-ray source, and 300- to 1,800-s live time. The spatial resolution for each measurement was 80–100 μm/pixel for all samples except one, where we increased the resolution to 28 μm/pixel to better constrain the scale of the subpixel mixing

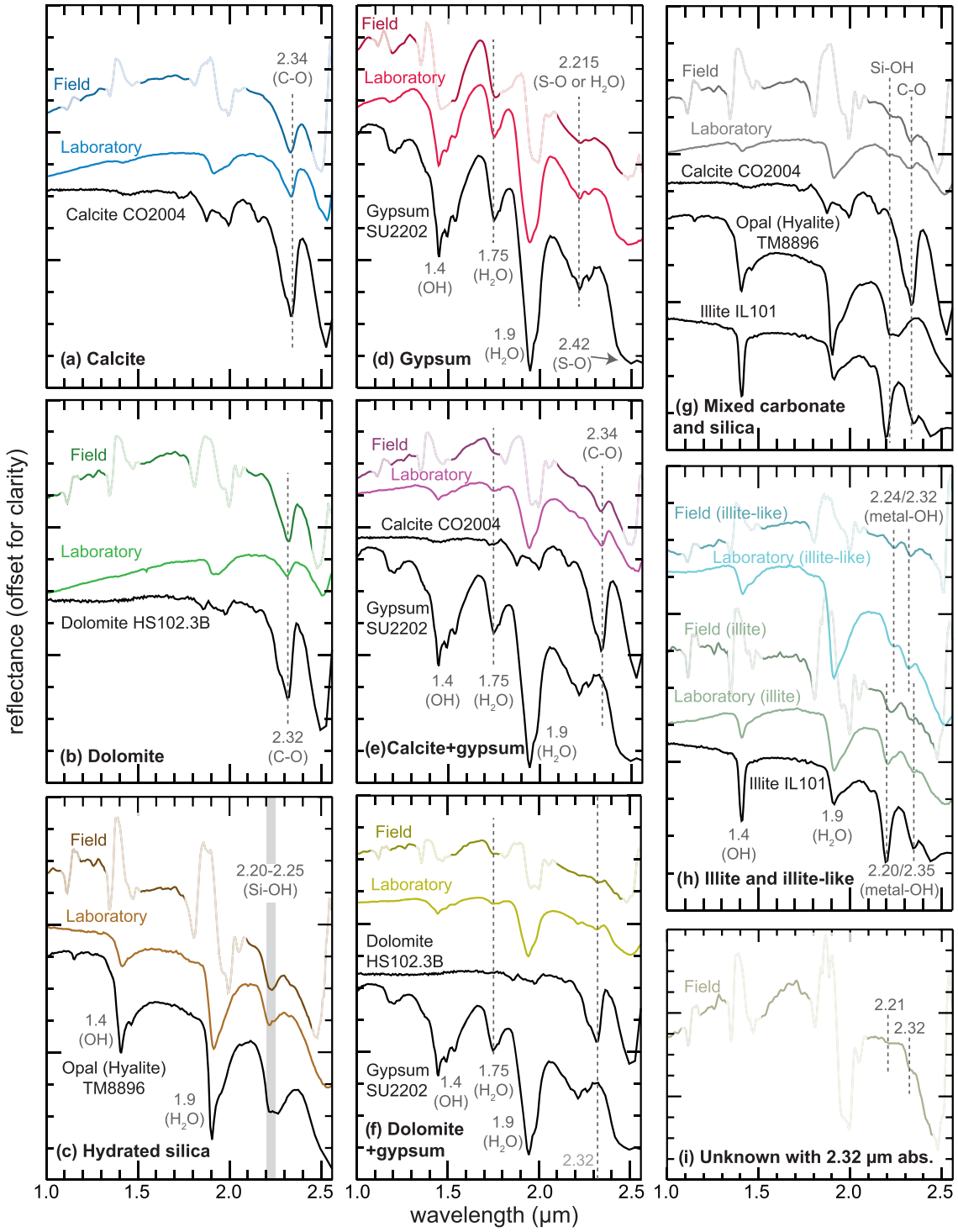

Figure 4. Infrared reflectance spectra of the main lithologies present from imaging spectroscopy measurements of laboratory samples (lighter colors) and outcrops (darker colors). Spectra are 5 × 5 averages. Spectra of pure endmember minerals from the USGS spectral library are shown in black for comparison (Clark et al., 2007). For field data, regions of atmospheric water vapor absorption resulting in little to no incident solar illumination have been masked and are mostly transparent. Lithologies shown are (a) calcite, (b) dolomite, (c) hydrated silica, (d) gypsum, (e) calcite + gypsum, (f) dolomite + gypsum, (g) mixed carbonate and silica, (h) illite and illite-like spectra, and (i) an unknown material with a 2.32-μm absorption feature.

Table 4
Classification Criteria for Each Lithologic Unit

Lithologic classification	Source depth (km)	Mineral indicators present	Mineral indicators absent	Other criteria
Calcite	0.5–1.9	Calcite	Hydrated silica 1 and 2, illite, illite-like, gypsum	Calcite > dolomite
Calcite + gypsum	0.5–1.9	Calcite, gypsum	Dolomite, illite, illite-like	
Dolomite	0–1.9	Dolomite	Hydrated silica 1 and 2, gypsum, illite, illite-like	Dolomite > calcite
Dolomite + gypsum	0–1.9	Dolomite, gypsum	Illite, illite-like	(Max of BD2220_2, BD2230) < 0.09
Carbonate + Si-OH	0–1.9+, melt	Calcite, dolomite, or unknown with 2.32-μm absorption; hydrated silica 1 or 2	Gypsum, illite, illite-like	None
Gypsum	0.9–1.1	Gypsum	Calcite, dolomite, illite, illite-like	(Max of BD2220_2, BD2230) < 0.09
Hydrated silica + gypsum	>0.9	Hydrated silica 1 or 2, gypsum	Calcite, dolomite	(Max of BD2220_2, BD2230) > 0.09
Hydrated silica	>1.3	Hydrated silica 1 or 2	Gypsum, calcite, dolomite, illite, illite-like, unknown with 2.32-μm absorption	None
Illite	1.6–1.7	Illite	(other classifications prevent overlap)	(Max of BD2200_illite, BD2200_illite2) > BD2240_illite
Illite-like	1.6–1.7	Illite-like	(other classifications prevent overlap)	BD2240_illite > (max of BD2200_illite, BD2200_illite2)
Unknown with 2.32-micron absorption	?	Unknown with 2.32-μm absorption	Calcite, dolomite, hydrated silica 1 and 2, gypsum, illite, illite-like	None
Unclassified	—	None	Calcite, dolomite, hydrated silica 1 and 2, gypsum, unknown with 2.32-μm absorption, illite, illite-like	None

Note. Criteria use mineral indicators in Table 3 to construct classes. Multiple minerals may be present within single pixels and cataloged if they exceed the thresholds from Table 3. These thresholds generate the groupings used to classify lithologies for Step 5 of Figure 3.

seen in imaging spectroscopy data. All cut samples were also imaged and analyzed via imaging spectroscopy following the same methods described in sections 3.2 and 3.3.

The XRF outputs are in units of counts/area, and counts at a specific keV increase linearly with elemental abundance. Different clasts within these samples have dramatically different compositions easily differentiated visually by the presence or absence of various elements; consequently, precise elemental abundances are unnecessary for identification of rock types to validate the imaging spectroscopy data. Standards analyzed with the same matrix and density as each component could provide a means of obtaining more exact element concentrations but are challenging to obtain for such heterogeneous samples, were not necessary, and, therefore, were not run.

4. Results

The impact melt rock at Haughton typically comprises a light gray groundmass with mm- to cm-sized clasts of various lithologies, most of which vary from white to dark gray/black. Occasional light green clasts are observed, as are periodic red coatings from oxidation to iron oxides. The rock types of clasts can sometimes be distinguished visually (e.g., gneiss), while other times are difficult due to the small sizes of many of the clasts. The clasts are mostly carbonate (limestone and dolostone), sandstone, gneiss, phyllosilicate, and evaporitic (gypsum or layered gypsum and carbonate). Rare lithologies include mafic clasts, and garnets are sometimes observed within the gneiss. These visual observations are consistent with Osinski, Spray, and Lee (2005) and all other previous work at Haughton.

4.1. Spectral Signatures of Major Lithologies

The major lithologies present at the Haughton impact structure and identified via spectroscopy are (1) calcite, (2) dolomite, (3) gypsum, (4) hydrated silica (often in sandstone or gneiss), (5) a phyllosilicate with absorption band centers consistent with illite, and (6) a similar spectrum to (5) but with offset absorption feature positions (termed “illite-like”), and mixtures ([7] calcite + gypsum, [8] dolomite + gypsum, [9] hydrated

silica with minor gypsum, and [10] hydrated silica + carbonate), and (11) an unknown material exhibiting an absorption feature at 2.32-μm distinct from carbonate (Figure 4; Table 4). Mafic lithologies and shales are uncommon, consistent with mapping by Osinski, Lee, Spray, et al. (2005).

Calcite (limestone; Figure 4a) and dolomite (dolostone; Figure 4b) both contain absorption features at 2.32–2.34 μm (third overtone of the asymmetric C-O stretch) and 2.5 μm (C-O combination) (Hunt & Salisbury, 1971). The two minerals in the two lithologies are distinguished by a shift in the overtone from ~2.32 μm in dolomite to ~2.34 μm in calcite (Gaffey, 1987). Shifts in absorption band center for the 2.5- to 2.55-μm band are also seen in laboratory measurements of Haughton samples and are consistent with the literature (Gaffey, 1987); however, attenuation by atmospheric water vapor makes this feature difficult to resolve beyond a downturn toward 2.5 μm in field data.

A broad absorption feature due to Si-OH at 2.21 μm is observed in silica-rich lithologies (Figure 4c), specifically sandstone and gneiss identified by visual examination at the outcrop-scale and in the laboratory. This Si-OH feature has been reported in quartz with minor amounts of water (Aines & Rossman, 1984) as well as in amorphous silica, such as opal (Anderson & Wickersheim, 1964; Goryniuk et al., 2004). Here, the silica-rich lithology includes quartz (unshocked or lightly shocked) to amorphous shocked silica generated by the impact event.

Gypsum is also common (Figure 4d). In laboratory data, it is characterized by a triplet of absorption features due to H_2O overtones at ~1.4–1.6 μm and a deep H-O-H combination at 1.94 μm (S-O or OH/H_2O) (Clark et al., 1990; Cloutis et al., 2006; Hunt et al., 1971). In field data, the shorter wavelength portion of the 1.4-μm triplet is obscured by atmospheric water vapor, though the continuation of the feature to longer wavelengths is observed, and the 1.9 μm is rarely seen for the same reason. Other spectral features of gypsum at 1.75, 2.21, and 2.26 μm due to S-O or OH/H_2O are observed in both laboratory and field spectra (e.g., Clark et al., 1990; Cloutis et al., 2006; Hunt et al., 1971).

Two phyllosilicate lithologies are present and are spectrally distinct (Figure 4h). The first has absorption band minima at 2.20 and 2.35 μm due to metal-OH combination features, consistent with illite/muscovite (Clark et al., 1990, 2007). The second has band centers at 2.23–2.24 and 2.31–2.33 μm. The band centers are similar to vermiculite (Clark et al., 1990), though the absorption feature shapes and relative band strengths differ, and the spectra lack an additional absorption at 2.39 μm. Based on XRF analyses, this lithology contains Si, K, and Fe but lacks Ca, suggesting that the longer wavelength absorption feature is not due to carbonate. These clasts are most likely either a phyllosilicate with an intermediate composition not represented in spectral libraries or an illite with Fe-OH, Mg-OH, and Al-OH bonds affected by shock processes. Friedlander et al. (2015, 2016) found that shock processes affect the octahedral and tetrahedral sheets of phyllosilicates differently and as a function of cation composition.

Another unknown material exhibits a spectral feature at 2.32 μm that differs in shape and position from carbonates, and the slope of the spectrum is always negative on the long wavelength side of the feature (Figure 4i). There may be a small amount of carbonate mixed with other materials, or the feature may be due to a weak signature from an unknown phyllosilicate, possibly poorly crystalline. We map this lithology spectrally to track its concentration in the melt rock but are unable to assign it to a specific mineral composition since it is not present in our collected samples.

As is common in natural rocks, minerals are often mixed at a sub-pixel spatial scale in both field and laboratory samples. Pixels containing both a carbonate and gypsum (Figures 4e and 4f) are evident by the presence of a broader 1.4-μm OH overtone and a feature at 1.75 μm (Clark et al., 1990; Hunt et al., 1971) along with an absorption at 2.32–2.34 μm, of which the exact wavelength of the minimum is indicative of the precise carbonate mineral (i.e., calcite—Figure 4e—or dolomite—Figure 4f). Some spectra have absorption features at both ~2.2 and 2.30–2.35 μm but are inconsistent with illite due to the band centers, widths, and/or relative depths (see library illite spectrum for comparison in Figure 4g). We interpret these spectra as silica-rich (quartz or amorphous) and carbonate subpixel mixtures (Figure 4g). Previous work has shown that the matrix of the melt contains hydrated silicate glass, carbonate, and anhydrite melt phases exhibiting liquid immiscibility textures at a scale below the spatial resolution of the imaging spectrometer (e.g., Osinski & Spray, 2001, 2003), resulting in spectra that fit in this class. Finally, there is a group of mixed pixels containing mostly Si-OH-bearing material (sandstone or gneiss) with a small proportion of gypsum, where the depth of the 2.20- to 2.25-μm feature is deeper than library spectra of pure gypsum and therefore requires the presence of Si-OH.

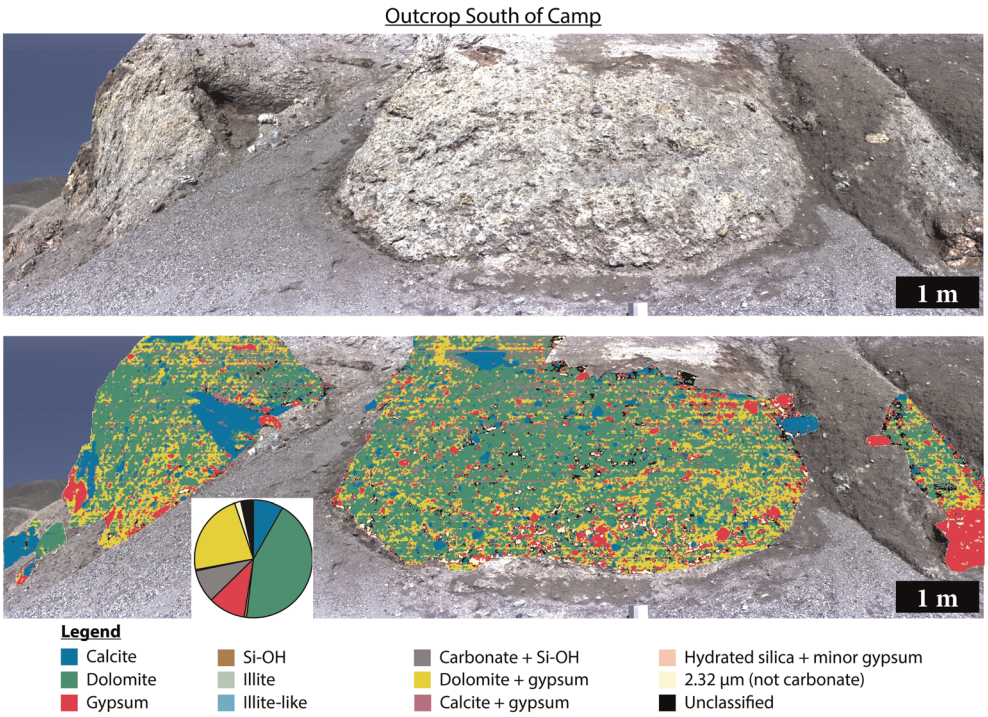

Figure 5. (Top) True color composite image from imaging spectroscopy data of the southernmost outcrop (south of camp). (Bottom) Lithologic mapping of outcrop compositions and pie chart with areal abundances of each lithology. The spatial resolution at the calibration target is ~7 mm/pixel, and spatial resolutions coarsen with increasing distance from the sensor.

A few other minor minerals and lithologies are identified in isolated occurrences as their own clasts or as a minor (<~5% area in laboratory samples) component in the melt-bearing breccia samples. These are mostly seen in laboratory data due to the increased spatial resolution and smaller size of the samples, and we estimate that they comprise <~1% of the outcrops. For example, garnet is present in many gneiss clasts and has a distinct set of crystal field absorption features (Burns, 1993; Izawa et al., 2018), and mm-size prehnite is rarely seen. Occasional mafic clasts are present (see SOC_C2_2 on Figure S1) and are dark with electronic transitions due to Fe^{2+} in primary minerals such as olivine and pyroxene and vibrational absorption features from varying amounts of water, likely minor weathering products. Iron oxides are also present and stain some clasts, particularly gneiss. The iron oxides are mostly transparent in the infrared, meaning that absorption features due to the minerals underneath are still observed (e.g., Singer, 1980).

4.2. Imaging Spectroscopy of Outcrops in the Field

All outcrops contain clasts of diverse composition found near each other and without evidence for size or density segregation. The outcrop south of camp (Figure 5; Table A1) contains abundant dolomite (43.7% area) with calcite (8.2%) limited to individual clasts scattered through the outcrops. Gypsum is also present on its own (10.2%) and mixed with dolomite (22.7%). There is a moderate amount of mixed Si-OH and carbonate lithologies (9.0%). Si-OH (not mixed with carbonate) is nearly absent (<1%), and no phyllosilicates are detected in the outcrop.

The Pinnacle outcrop (Figure 6; Table A1) is compositionally stratified. The lower portion of the outcrop is primarily calcite, while the upper portion is a mixture of calcite and gypsum or, toward the top, dolomite and gypsum. Dolomite (1.5%) rarely occurs in large enough areas or clasts to fill its own pixels and nearly always occurs in the same pixels as gypsum. Gypsum (2.3%) similarly rarely occurs without a carbonate at the subpixel scale. There is little Si-OH or phyllosilicate in this outcrop.

At Rhinoceros Creek (Figure 7; Table A1), mixed Si-OH and carbonate are the highest areal abundance lithology (41.6%) followed by calcite (31.2%). Calcite is ~4× more abundant than dolomite (7.2%). Significant material exhibiting a Si-OH absorption feature (gneiss and sandstone) without carbonate is

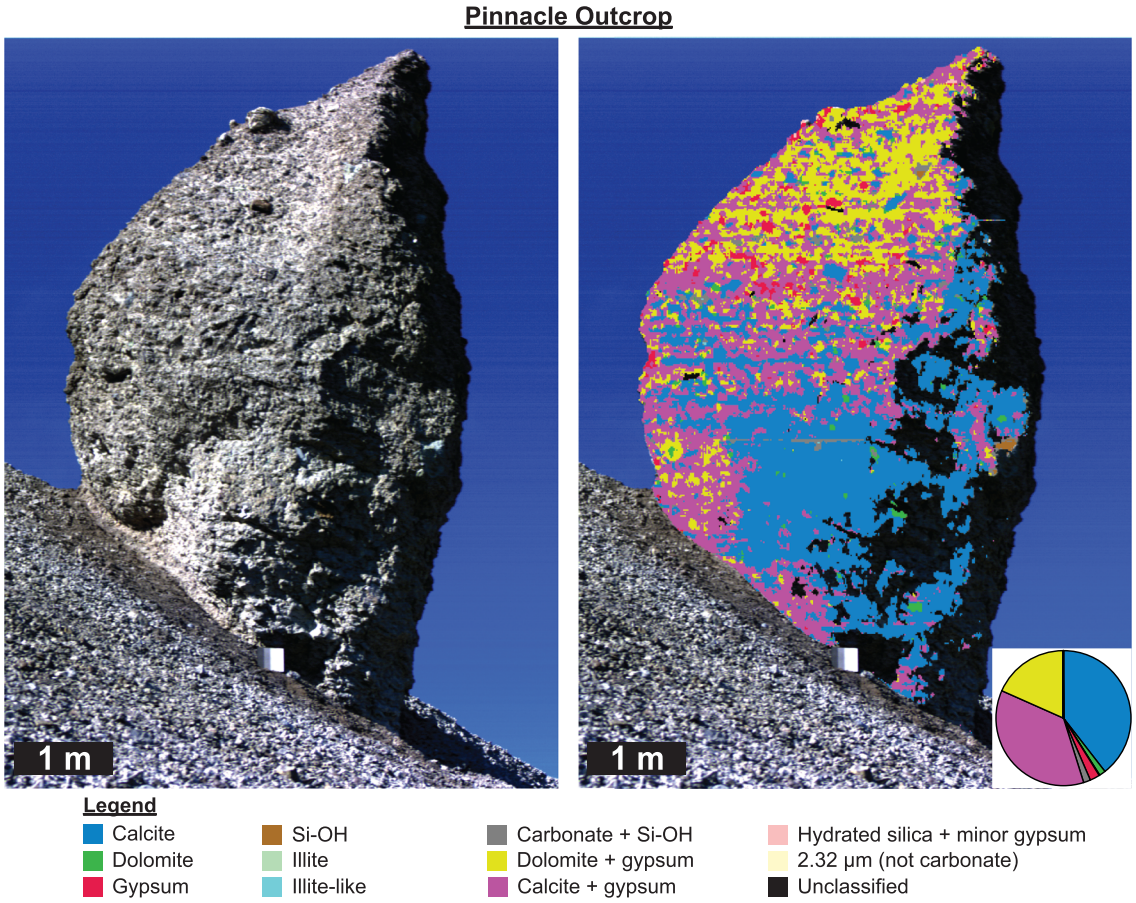

Figure 6. (Left) True color composite image from imaging spectroscopy data of the Pinnacle outcrop. (Right) Lithologic mapping of outcrop compositions and pie chart with areal abundances of each lithology. Shadows have been masked and removed from areal abundance calculations. Nearly all dark areas in the image are shadows, not formally unclassified pixels. Spatial resolution at the calibration target is ~1.3 cm/pixel.

also present (9.2%), as are phyllosilicates (8.3%), with more of the "illite-like" lithology observed. There is essentially no gypsum, with or without carbonate.

Less-than-ideal sky conditions and low solar elevation precluded use of the field images from the overhang south of Rhinoceros Creek and the creek south of Rhinoceros Creek because of the images' low signal-to-noise, and we do not discuss these images further. Interestingly, samples collected from the creek south of Rhinoceros Creek outcrop (Section 4.3) are more "noisy" as well. There may be a matrix or compositional effect reducing the strength of absorption features within the rocks at this particular outcrop in addition to the non-ideal acquisition conditions (see section 3.1 and Table 1).

Bruno Escarpment changes in composition along its length from calcite-rich to areas with more gypsum and dolomite and eventually some Si-OH signatures (Figure 8). Quantitative abundances were not determined for this outcrop due to it being highly weathered and the coarse spatial resolution of the measurement, compared to the pristine melt rock outcrops (Figures 5–7). Overall, based on examination of individual spectra and our knowledge of the escarpment, we have confidence in the major compositional changes that are mapped in Figure 8 and in large, spatially coherent areas that map as a single lithology. Mineral detections in small areas and in few pixel regions are less certain.

4.3. Laboratory Imaging Spectroscopy

Single clasts collected in the field encompass fully the lithologies identified at the outcrop scale. They generally map as a single mineral at >90% abundance (calcite, dolomite, Si-OH, or gypsum) or up to 61.5% illite and/or the "illite-like" phyllosilicate (Figure S1; Table A2). We collected some rare lithologies such as mafic clasts that are not observable at the outcrop scale.

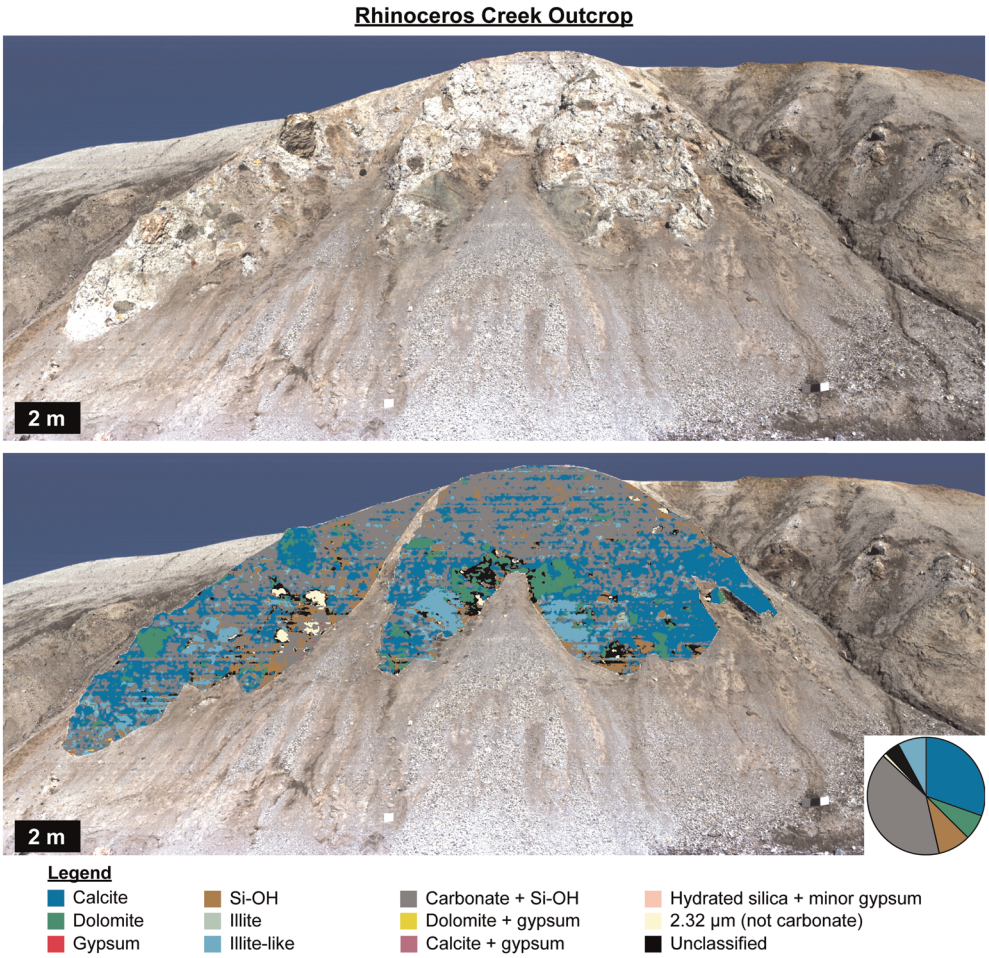

Figure 7. (Top) True color composite image from imaging spectroscopy data of the Rhinoceros Creek outcrop. (Bottom) Lithologic mapping overlain on the outcrop and pie chart showing areal abundances of each lithology. Spatial resolution at the calibration targets is 2.5–2.7 cm/pixel. At the top of the outcrop, spatial resolution is decreased by a factor of ~2, yielding a resolution of ~5–5.5 cm/pixel.

Breccia-type samples of the melt rock nearly always have multiple lithologies identified within each sample (Figures 9 and 10; Table A2). Comparisons of samples cut for XRF analyses where both the back and front were imaged agree, with median difference of 0.5% in areal abundance for all phases (Figure 9). Larger areal differences up to 19% only occur where large clasts are exposed on one side and not the other simply due to the placement of the cut. Consequently, lab data verify the consistency of the mapping algorithm.

Within the polymict breccia-type samples, the dominant lithologies vary from outcrop to outcrop. Gypsum, dolomite, and dolomite + gypsum lithologies are the dominant phases in samples from the outcrop south of camp and the overhang south of Rhinoceros Creek with very few silicates (Si-OH, illite, "illite-like," and mixed Si-OH lithologies) (Figure 10; Table A2). Calcite, dolomite, gypsum, and their mixed lithologies with little Si-OH or phyllosilicate are characteristic of upper Pinnacle; and lower Pinnacle is almost entirely calcite and dolomite, with the exception of one large gypsum clast (Figure 10; Table A2).

Silicates are more common at other locations. Calcite, dolomite, mixed carbonate and Si-OH, Si-OH, and phyllosilicates are all common with little gypsum in the Rhinoceros Creek outcrop. A green spur at Rhinoceros Creek (Figure S1; C6_1–4 and C7_1 on Table A2) contains 11.7–60.7% of the "illite-like" lithology. Areal abundances of calcite, dolomite, gypsum, illite, and mixed carbonate and Si-OH can all be high but vary significantly sample to sample for the overhang south of Rhinoceros Creek outcrop and the Western outcrop (Figure 10, Table A2).

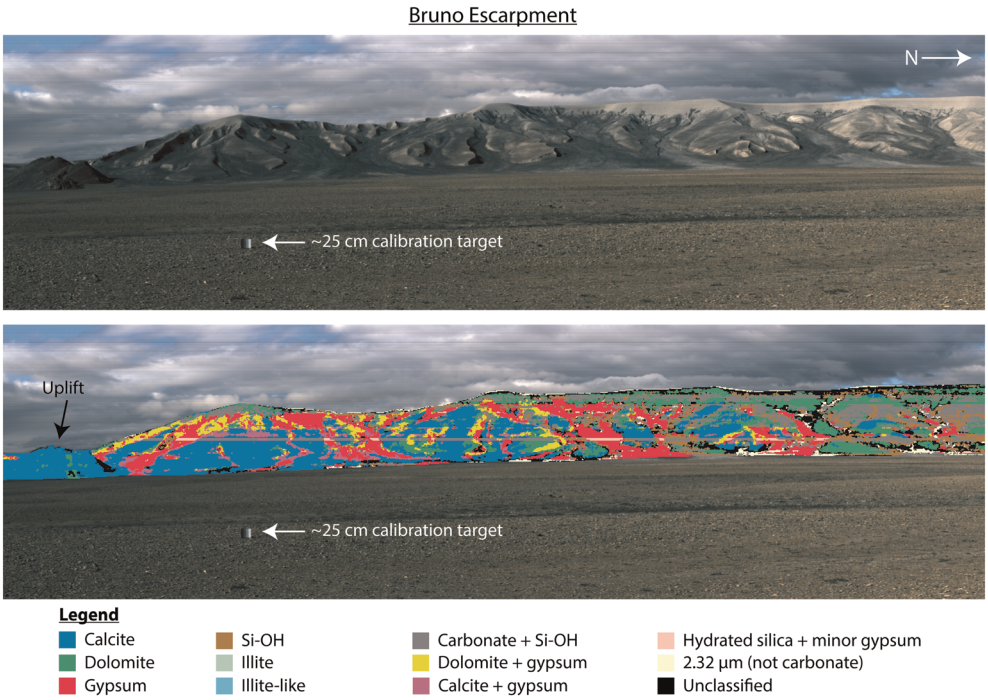

Figure 8. (Top) True color composite image of Bruno Escarpment, which is a weathered and eroded escarpment of melt rock. (Bottom) Composition overlain on the escarpment. This image covers ~1–1.5 km in lateral distance. An outcrop of uplift of the Eleanor River Formation is marked on the left and consists mostly of a dark limestone; the remainder of the escarpment is weathered melt rock. The image was taken at a distance of 1–1.5 km from the outcrop, and average spatial resolution is estimated to be on the order of 1–2 m/pixel.

4.4. XRF Compositional Mapping

XRF semiquantitative mapping validated the imaging spectroscopy data (Figures 11b and 12b). Clasts with the highest XRF Ca counts are calcite; clasts with intermediate Ca counts and no S are dolomite; and clasts with lower Ca counts and S are gypsum, matching mapping from imaging spectroscopy. Gypsum has a higher percentage of Ca than dolomite but is less dense, so the Ca per area is lower. Gypsum is at times more prominent in the SWIR data, particularly where small silica-bearing (sandstone or gneiss) clasts are adjacent to or embedded within gypsum, likely due to the transparency of silica at SWIR wavelengths, so this may lead to a minor gypsum overestimation (Figure 11).

Pixels that map as Si-OH in imaging spectroscopy have high XRF Si counts with no Fe or K and are thus quartz or shocked quartz (now amorphous silica). Small regions of very high Fe are iron oxides or sulfides. Local areas classified as illite/illite-like with spectroscopy have Si, Fe, and K, consistent with illite or a similar phyllosilicate and the shale known to be in the target stratigraphy. Spectra of the groundmass that typically exhibit multiple features of dolomite, silica, and some illite/illite-like phyllosilicate are consistent with the low to moderate amounts of all elements measured with XRF, in agreement with backscattered electron imaging of the melt by Osinski and Spray (2001, 2003) that shows immiscible textures between the calcite and silica-rich glass. The groundmass micrometer-scale immiscible textures are well below the resolution of the imaging spectroscopy (~225 μm/pixel) and all XRF measurements (Figure 12c; up to 28 μm/pixel), so spectral classification as mixed carbonate and silica spectra, perhaps with some devitrified glass, is appropriate.

5. Discussion

5.1. Heterogeneity of Impact Melt

5.1.1. The Outcrop Scale

The dramatic compositional differences measured in the field from outcrop to outcrop (Figures 5–12) support the conclusion that the crater-fill impact melt deposit at Haughton is heterogeneous. Previous work

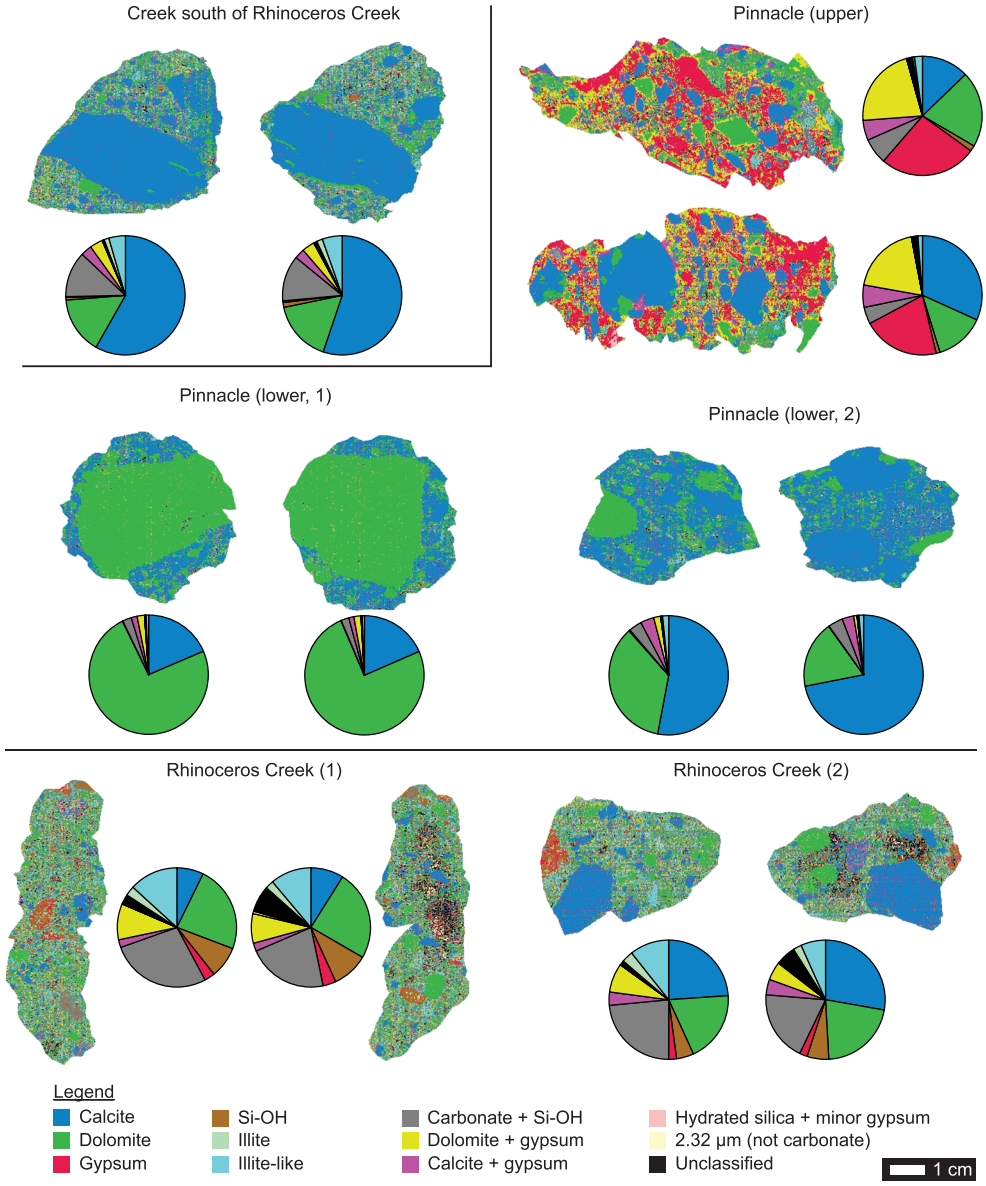

Figure 9. Lithologic maps of both sides of samples cut for XRF analyses and pie charts show that computed areal abundances of each lithology determined via imaging spectroscopy are similar for both sides of the sample. Spatial resolution in these images is ~225 μm/pixel.

at Haughton reached a similar qualitative conclusion for the clast population of the melt rock (Osinski et al., 2008; Osinski, Spray, & Lee, 2005; Redeker & Stöffler, 1988). For the first time, we have quantified the magnitude of large outcrop-to-outcrop variation for both the clasts and groundmass that compose the impact melt at different spatial scales (see section 5.1.2). In field data, quantitative areal abundances vary between outcrops by more than 40% for some lithologies. Outcrop-to-outcrop differences in hand samples show similar trends as the outcrop-scale field imaging spectroscopy results (Figures 13 and 14). However, hand samples also vary in composition within single outcrops, sometimes by 10s of percent in areal abundance, and between samples and the outcrops from which they were collected (Figures 13 and 14). This result validates our approach; attempting this study solely through sample collection-based methods would likely not yield accurate outcrop-scale compositions because of the sample-to-sample variability. Therefore, while laboratory validation and calibration through sample analyses are essential components of this work, quantification of the heterogeneity is enabled by compositional measurements of full outcrops.

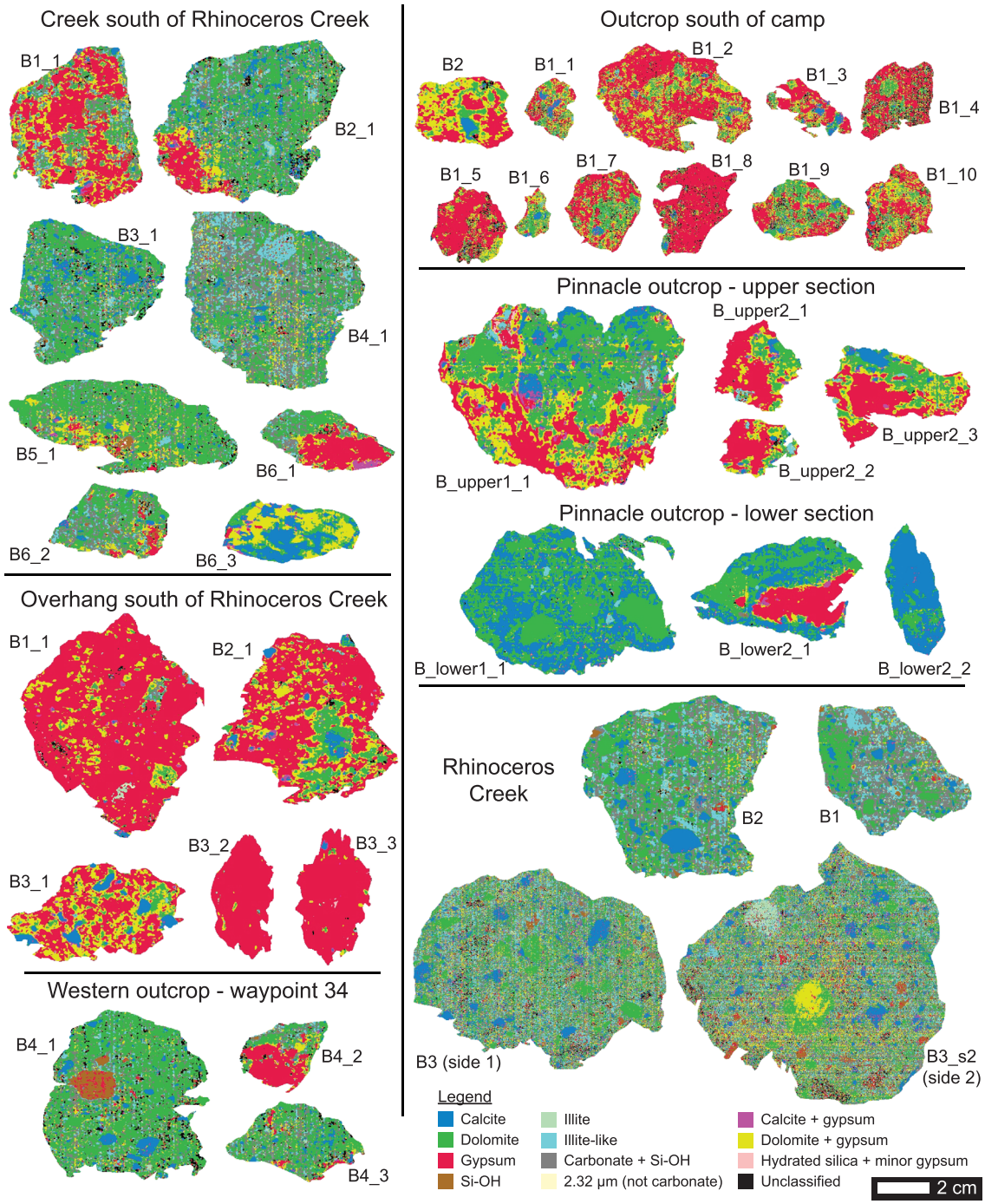

Figure 10. Lithologic maps from imaging spectroscopy of polymict clast-rich impact melt rock (breccia) samples collected from six outcrops at the Haughton structure.

Laboratory and field spectra of the lithologic types agree (Figure 4). Minor differences in the relative strengths of absorption features for mixed lithologies are due to differences in the relative abundances of the minerals. Importantly, the compositional differences at outcrop scale are present at the hand sample scale. Calculating the median spectrum of hand samples to approximate the centimeter-scale spatial resolutions of outcrop images (Figure 15) shows clear differences that match the trends seen in outcrop-scale imaging (Figure 13; Tables A1–A2) with, e.g., the outcrop South of Camp having more gypsum than the carbonate- and silica-dominated Rhinoceros Creek outcrop.

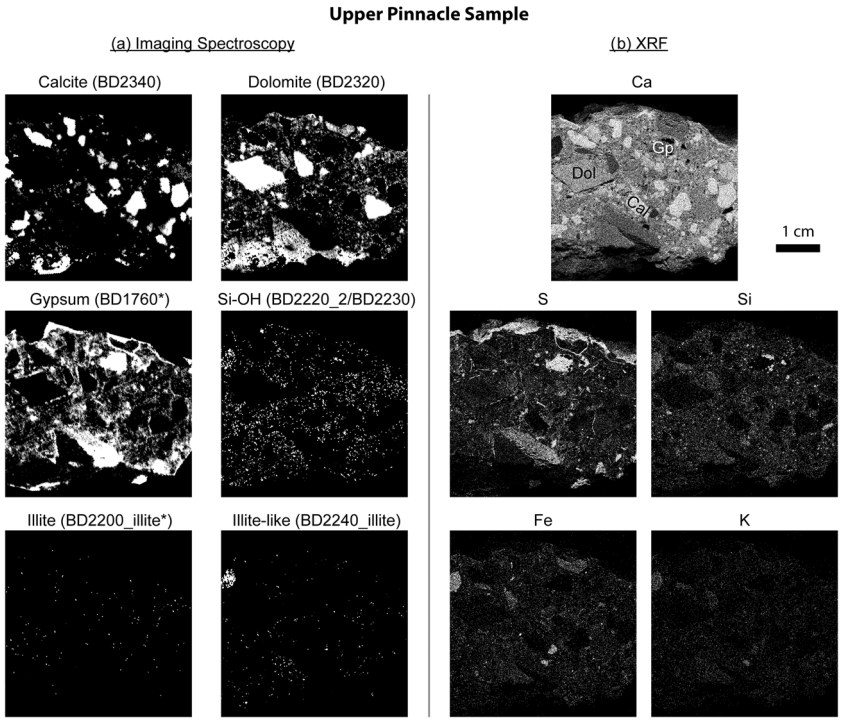

Figure 11. (a) Compositional maps derived from imaging spectroscopy of cut sample Upper_s1 from the Pinnacle outcrop. Each panel uses a mineral indicator from Table 3 to determine the presence or absence of each lithology, and the displayed values and grayscale intensities shown are the depth of a key absorption feature from each lithology (see Table 2 for formulas) where the given mineral indicator is positive (*BD1760 refers to the maximum of BD1760_narrow_field and BD1760_field, and BD2200_illite refers to the maximum of BD2200_illite and BD2200_illite2). (b) Maps of elemental composition determined via XRF for the same sample, where black is absent and white is highest. The linear stretch applied to images for each element is identical to Figure 12. Cal = calcite, Dol = dolomite, and Gp = gypsum.

The compositional heterogeneities are preserved at larger scales as well. At the Rhinoceros Creek outcrop, sensor-to-outcrop distances vary by a factor of up to 2–2.5×, as measured with a laser range finder. While the difference in spatial resolution may lead to identification of more mixed pixels (carbonate + Si-OH, gypsum + calcite, gypsum + dolomite, and gypsum + hydrated silica), it does not affect the presence or absence of lithologies within mixtures. The near total absence of gypsum or gypsum mixtures observed at Rhinoceros Creek and in samples collected from that outcrop cannot be explained by spatial resolution because gypsum is absent in mixed lithologies at all scales (Figures 13 and 14). In addition, a test artificially decreasing the spatial resolution of the Pinnacle image by a factor of 4 results in only minor changes in areal abundances of calcite (−9.1%) and gypsum (−1.9%) and increases the proportion of gypsum + calcite, retaining evidence for the presence of both gypsum and calcite. Furthermore, if coarser resolution and subpixel mixing explained the absence of phases rather than true spatial heterogeneity, the higher spatial resolution image of the Pinnacle outcrop should contain all lithologies at Rhinoceros Creek. However, nearly no pixels contained lithologies with hydrated silica (gneiss and sandstone) or phyllosilicates (illite or illite-like) at Pinnacle (Figure 14). Therefore, the quantitative trends from site to site observed in the data are real: large differences from outcrop to outcrop can only be explained as real differences in melt rock composition.

5.1.2. Heterogeneities Within the Groundmass

While clasts are an important tracer, the groundmass is equally or more important, as the melt is entirely contained within the groundmass. We use the same definition of groundmass as Osinski, Spray, and Lee (2005): “the fine-grained material that encloses fragments of shocked and unshocked target material.” Other studies have found heterogeneities within the groundmass of impact melt rock at the Ries impact structure (Siegert & Hecht, 2018) and in crystalline targets (Marion & Sylvester, 2010), though the nature of the groundmass differs in crystalline targets.

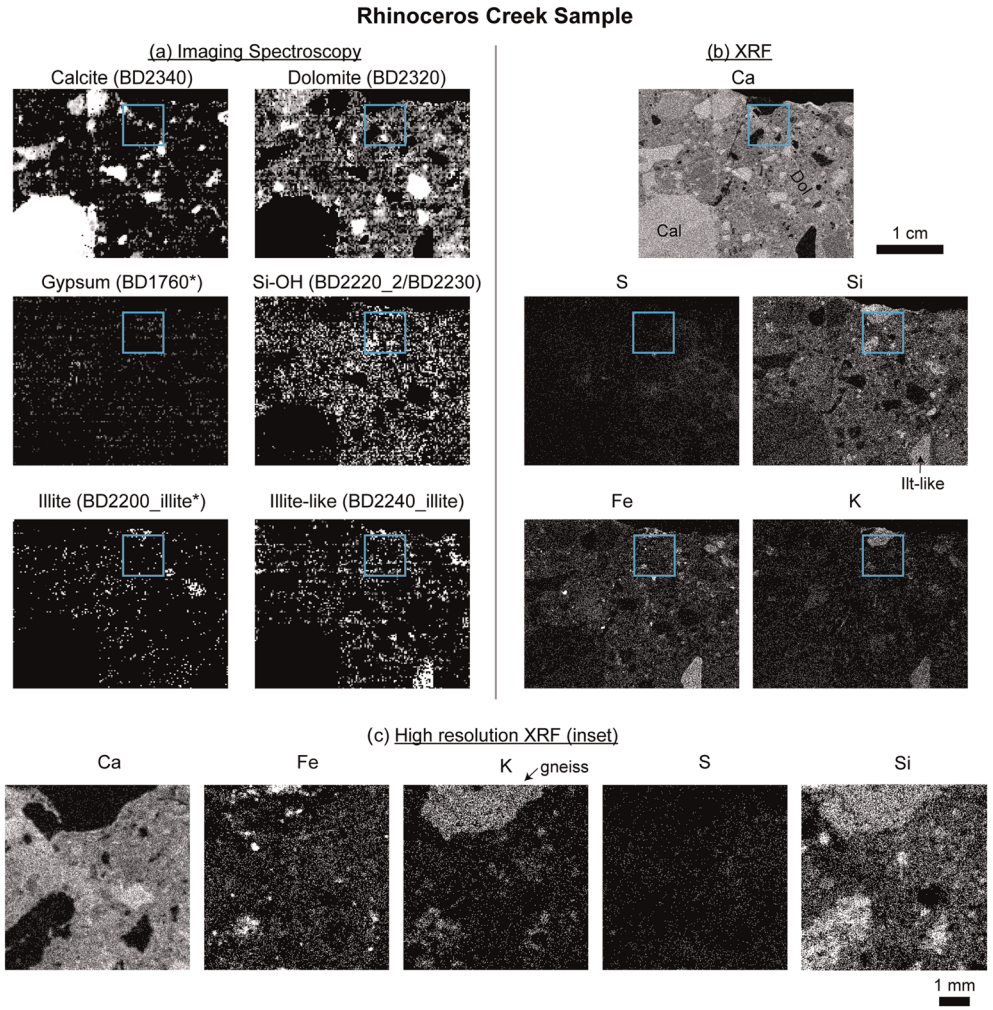

Figure 12. (a) Compositional maps derived from imaging spectroscopy of cut sample Small_S1 from the Rhinoceros Creek outcrop. Each panel uses a mineral indicator from Table 3 to determine the presence or absence of each lithology, and the displayed values and grayscale intensities shown are the depth of a key absorption feature from each lithology (see Table 2 for formulas) where the mineral indicator is positive. Displayed grayscale values are derived from the stated spectral parameters where that mineral indicator is positive (*BD1760 refers to the maximum of BD1760_narrow_field and BD1760_field, and BD2200_illite refers to the maximum of BD2200_illite and BD2200_illite2). (b) Maps of elemental composition determined via XRF for the same sample. (c) Higher spatial resolution maps of elemental composition for the portion of this sample in the blue boxes within (a) and (b) from XRF mapping, where black is absent and white is highest. The linear stretch applied to images for each element is identical to Figure 11. Cal = calcite, and Dol = dolomite.

At hand sample scale, our "mixed lithologies" (calcite/dolomite + gypsum; carbonate + Si-OH) coincide with the groundmass and are distinct from the spectral signatures of clasts (typically dominated by calcite, dolomite, gypsum, Si-OH, or phyllosilicate; Figure S1; Table A2). Heterogeneities of the groundmass parallel observed outcrop-to-outcrop variations in clast composition (Figure 14). The abundances of groundmass lithologies carbonate + gypsum and carbonate + Si-OH are distinct from outcrop to outcrop and vary inversely (Figures 13 and 14a): signatures of gypsum are apparent in spectra of the groundmass of a sample from the south of camp outcrop and Pinnacle outcrop and are weak to nonexistent in the groundmass of the sample from Rhinoceros Creek (Figure 16). This observation was validated with semiquantitative XRF, which shows lower S in the groundmass at Rhinoceros Creek (Figure 12). The same general trends scale from samples to outcrops (see squares in Figure 14a): the Rhinoceros Creek outcrop contains significant carbonate + Si-OH and little carbonate + gypsum, the south of camp outcrop has low but measureable

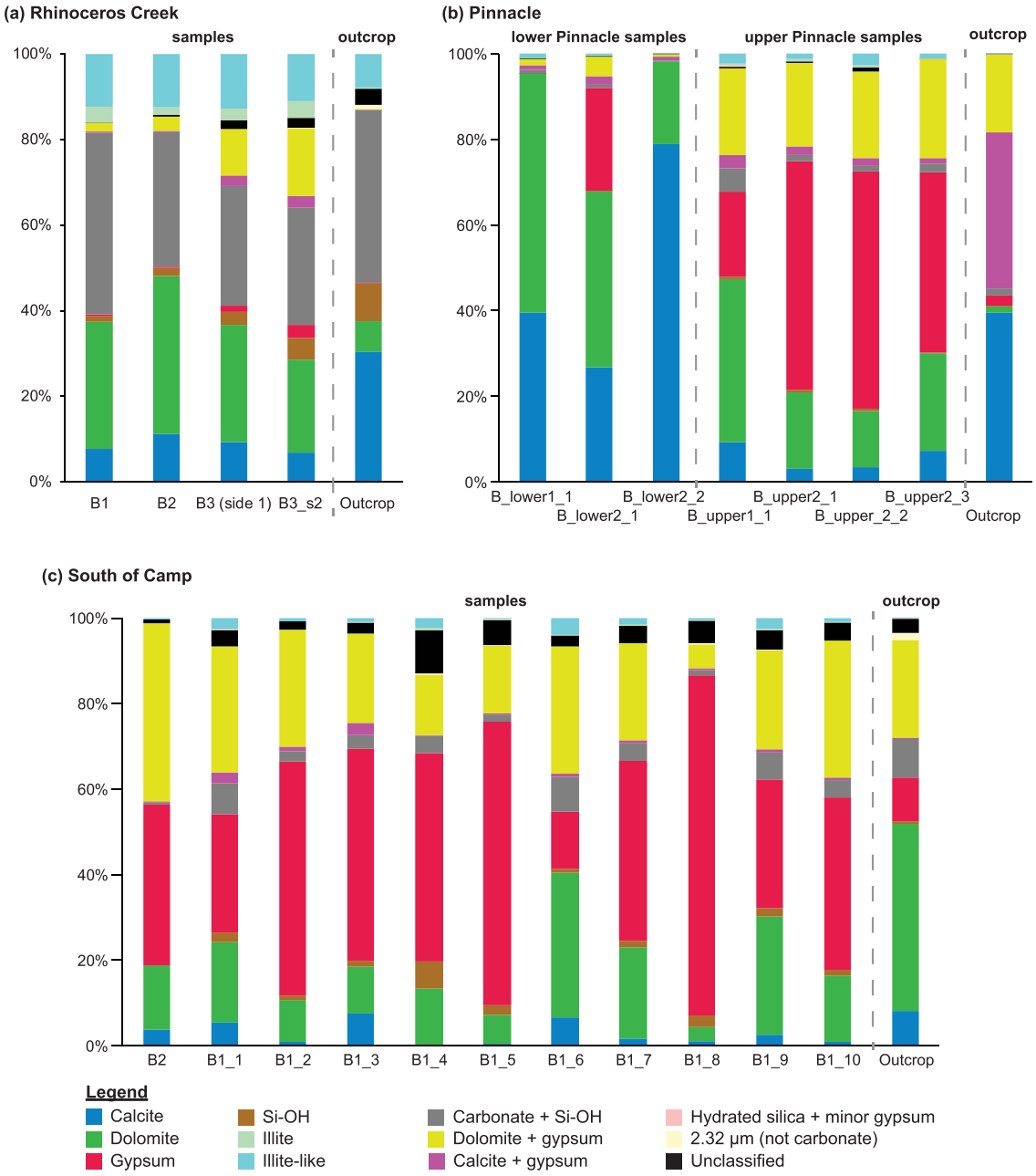

Figure 13. Bar plots showing areal abundances from imaging spectroscopy of each lithology in impact melt rock samples collected from outcrops (left) and within the corresponding outcrops imaged in the field (right) for (a) Rhinoceros Creek, (b) Pinnacle, and (c) South of Camp outcrops.

carbonate + Si-OH and higher carbonate + gypsum, and the Pinnacle outcrop has the highest carbonate + gypsum and little carbonate + Si-OH.

Thus, there are clear compositional differences in the groundmass at the outcrop-scale with location at the Haughton impact structure. For further quantification of the scale of compositional mixing, a microscopic study of 10s of melt samples or more per outcrop would also allow investigation of fine-grained clasts (10s of microns or smaller; Osinski, Spray, & Lee, 2005; Osinski & Spray, 2001, 2003) and melt separately.

5.1.3. Source Depths and Origins of Lithologies Within the Melt Rock

At Haughton, the lithologic sources for both clasts and groundmass exhibit consistent outcrop to outcrop trends. Si-OH-dominated (sandstone, gneiss, and to a lesser extent shale), phyllosilicate (illite and illite-like), and mixed carbonate + Si-OH lithologies are correlated in both the overall outcrop and hand

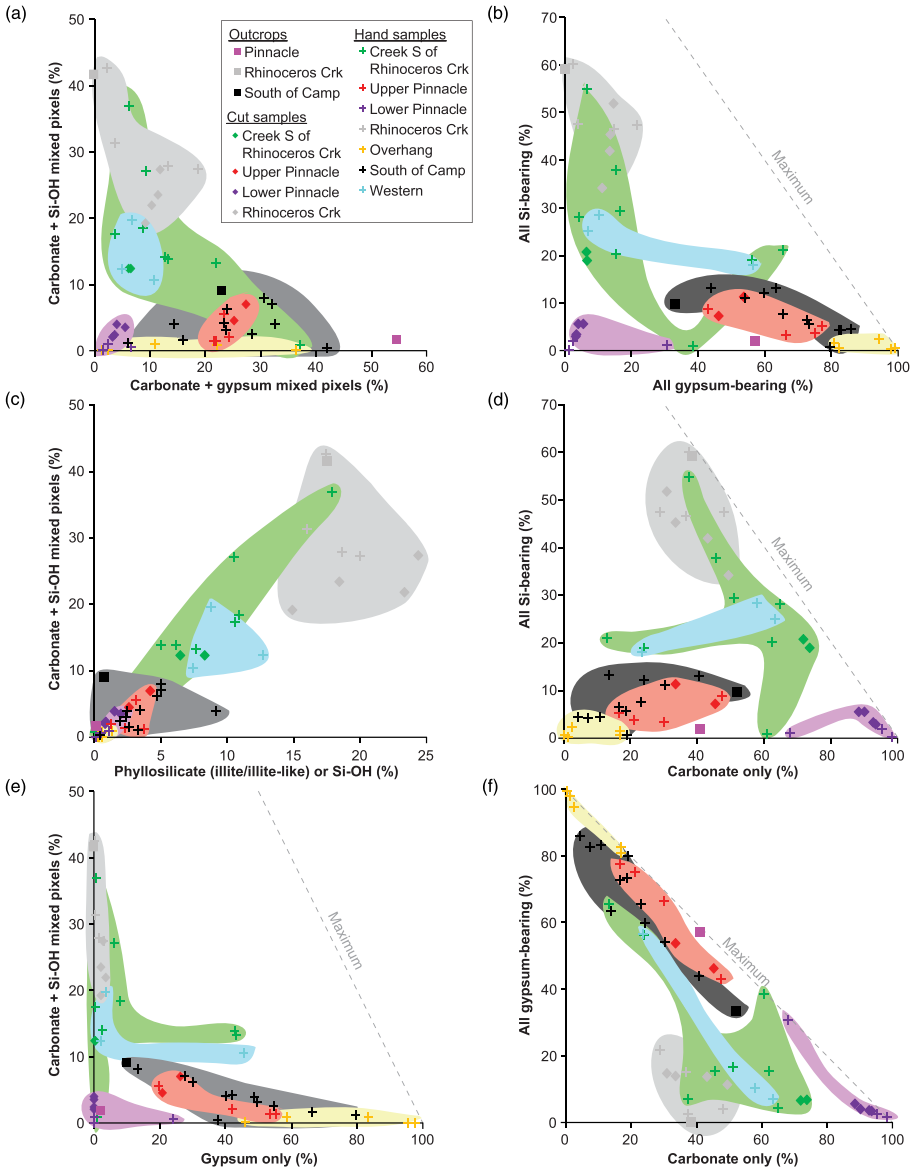

Figure 14. Scatterplots of lithologic compositions of samples cut for XRF analyses, uncut hand samples, and outcrops determined via imaging spectroscopy showing relationships in areal abundance between (a) carbonate + Si-OH versus carbonate + gypsum, both largely in the groundmass; (b) all Si-bearing lithologies versus all gypsum-bearing lithologies; (c) carbonate + Si-OH versus phyllosilicate or Si-OH bearing, (d) all Si-bearing versus pixels with only carbonate, (e) carbonate + Si-OH mixed pixels versus gypsum only, and (f) all gypsum-bearing lithologies versus carbonate only. Shaded regions were drawn to highlight points from the same outcrop. Symbols designate type of samples, while color is constant for different types of measurements from the same outcrop. "Carbonate + gypsum mixed pixels" is the total percentage of pixels classified as either "calcite + gypsum" or "dolomite + gypsum" (i.e., containing both carbonate and gypsum in the same pixel). "Carbonate + Si-OH mixed pixels" is the "carbonate + Si-OH" lithology. Lithologies followed by "only" are pixels with that mineral/lithology only and not another lithology (e.g., gypsum). "All Si bearing" are pixels classified as carbonate + Si-OH, Si-OH, illite, or illite-like. "All gypsum bearing" are pixels classified as gypsum, calcite + gypsum, or dolomite + gypsum. The maximum line shows where the two axes sum to 100%.

samples, and all exhibit an inverse correlation with gypsum (Figures 13, 14, and S3). Along the same lines, samples with >20% carbonate + Si-OH have little gypsum (Figure 14e), while samples with higher dolomite/calcite + gypsum generally have more gypsum without carbonate (Figure S3b; at the highest gypsum abundances, the abundance of carbonate + gypsum is low because the sample is nearly 100% gypsum). These lithologic tradeoffs are linked to known lithologies from different depths within the stratigraphy of the target rocks (Figure 2; Osinski, Spray, & Lee, 2005). Sandstone and

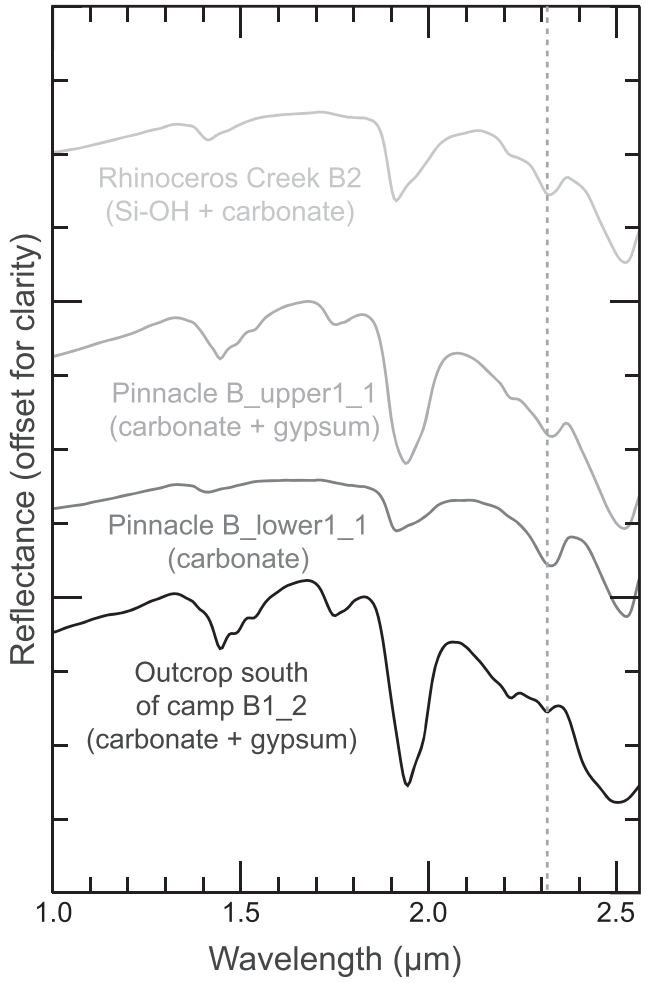

Figure 15. Median spectra of four hand samples imaged in the laboratory. The vertical gray guideline is at 2.31 μm. Spectral interpretations are given for each sample based on the median spectra, for comparison with Figure 13 and Table A1.

gneiss are sourced from the deepest target rocks, >1.3 km deep; phyllosilicate-bearing shales are mostly from 1.6 to 1.7 km depth. Gypsum, dominantly in the Bay Fiord Formation, is from higher in the target stratigraphy at 0.9–1.1 km depth and up to 1.5 km in minor amounts in the Blanley Bay formation (Figure 2). Calcite and dolomite occur throughout the <~1.8-km target stratigraphy. The fact that the target lithologies show systematic variations indicates that different depths are sampled by the melt rock at different locations within the crater (Figure 17).

At Rhinoceros Creek, total abundances of Si-bearing lithologies (phyllosilicate, Si-OH, and carbonate + Si-OH) are 34–60% in samples and 59% of the full outcrop. Conversely, lithologies containing gypsum from ~1-km depth are barely detected in the outcrop and are low (<~20%) in samples. As a result, we conclude that the bulk of this melt rock outcrop is sourced from >1.3-km depth, with a high proportion of sandstone and gneiss lithologies, most from the crystalline basement at >1.9 km.

Gypsum-bearing lithologies are common at the Pinnacle outcrop in both clasts (2–50+% gypsum) and groundmass (21–55% calcite + gypsum or dolomite + gypsum), while Si-bearing lithologies are uncommon (<2–12%). The high abundance of gypsum combined with the low proportion of silica and phyllosilicates suggests Pinnacle melt rock source depths of generally <1.1 km.

The southernmost outcrop contains both gypsum (33–86% gypsum or carbonate + gypsum) and Si-bearing (up to 14%) materials in clasts and groundmass. The melt rock at this locality appears to sample a wider range of depth of the target stratigraphy than the previous two outcrops.

While its compositions were not quantified due to the weathering and low spatial resolution of the imaging, similar to other outcrops, there are spatial distinctions between locations of gypsum and Si-OH along the ~1- to 1.5-km Bruno Escarpment that was imaged (Figure 8). The southernmost portion of the outcrop contains abundant calcite and is adjacent to the limestone of the Eleanor River Formation uplift (Figure 2; Osinski, Lee, Spray et al., 2005; Osinski, Spray, & Lee, 2005), suggesting local incorporation of material from the nearby uplift, as observed elsewhere at Haughton (Osinski, Spray, & Lee, 2005) and other impact structures (Grieve et al., 1977). However, proximity to uplift does not always control clast compositions; the gypsum-poor Rhinoceros Creek outcrop is adjacent to parautochthonous lithic breccias with large gypsum-rich Bay Fiord Formation clasts (see Fig. 3 of Osinski, Spray, & Lee, 2005) and a nearby Bay Fiord Formation uplift (Figure 2; Osinski, Lee, Spray et al., 2005).

From hand samples only of individual clasts and melt rock breccias, most of the remaining outcrops sample the complete stratigraphic column of the target rock (Figures 14 and 17; note that large gneiss clasts were observed visually and collected from the overhang south of Rhinoceros Creek—see Figure S1; Table A2).

One question is whether the outcrop-to-outcrop variation results from clast settling and differences in depths within the melt sheet as opposed to sampling different portions of the target stratigraphy. We suggest that clast settling is not the primary controlling factor here because it would generate significant differences in clast size for different lithologies at different outcrops, which are not observed. Furthermore, outcrop-to-outcrop variations are present at the hand-sample scale, and the clast size distribution is similar among samples from all outcrops.

Ideally, more comprehensive, outcrop-scale imaging spectroscopy in the field would be utilized to determine whether there is a coherent spatial pattern for melt rock composition at the Haughton impact structure.

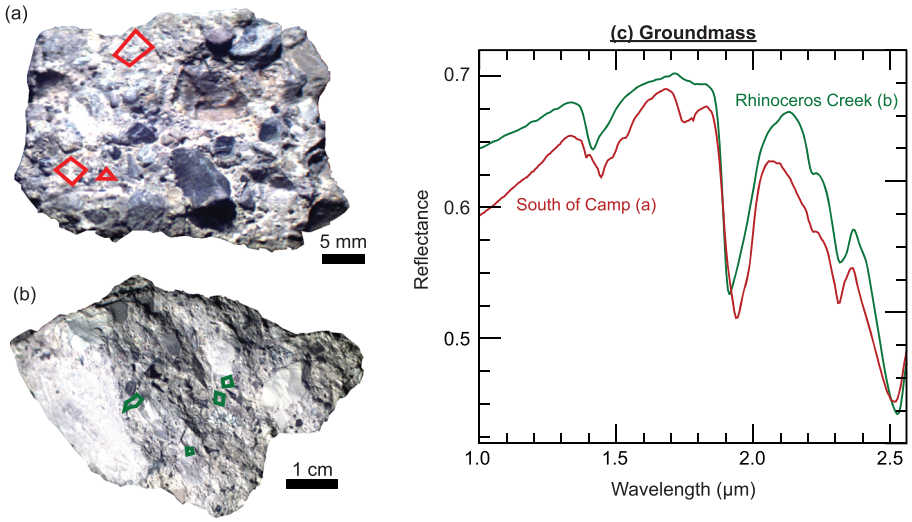

Figure 16. Approximate true color composite images derived from imaging spectroscopy measurements of (a) Sample B2 from the south of camp outcrop and (b) Sample B2 from Rhinoceros Creek. (c) Mean spectra of the groundmass of samples from the south of camp and Rhinoceros Creek outcrops. Locations averaged to produce each spectrum are outlined in red in (a) and green in (b).

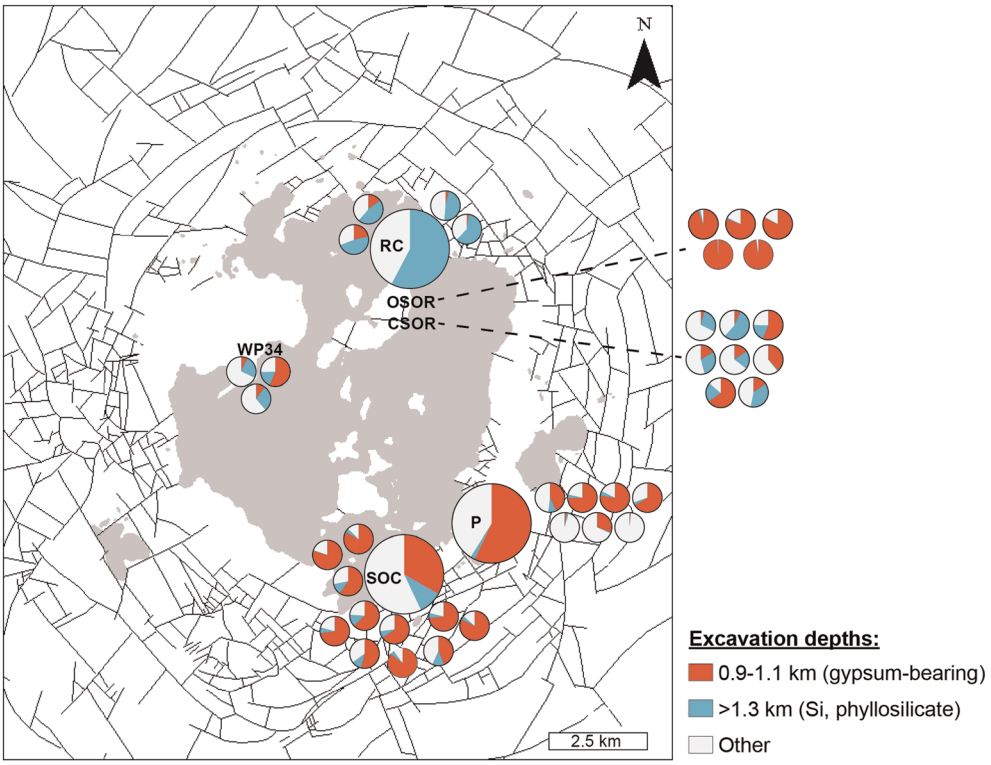

Figure 17. Map of the Haughton impact structure with faults (black lines) and the present-day extent of the impact melt rock (light gray) from Osinski, Lee, Spray, et al. (2005). Pie charts show the proportions of pixels containing lithologies from distinctly identifiable depths in images of outcrops (large circles) and samples (small circles): gypsum-bearing materials are sourced from 0.9–1.5 (almost entirely 0.9–1.1) km and Si-bearing (sandstone, gneiss, phyllosilicates) source from >1.3-km depth. The "other" category ismostly carbonate. Note that the gypsum and Si-bearing units often contain carbonates, which are from up to 1.8-km depth. P = Pinnacle. RC = Rhinoceros Creek. SOC = South of Camp. OSOR = Overhang South of Rhinoceros Creek. CSOR = Creek south of Rhinoceros Creek. WP34 = Waypoint 34 (westernmost outcrop).

These measurements were impossible during our field season due to the unexpectedly limited number of days with good sky conditions for data acquisition. It is possible that outcrops that are closer to the center of the structure sample a larger portion of the target stratigraphy (Figure 17), but dramatic compositional variations also exist among nearby or within single outcrops (e.g., within Pinnacle and the Bruno Escarpment). Previously, Osinski, Spray, and Lee (2005) noted the presence of gypsum/anhydrite clasts only in the eastern half of the structure and concentrations of highly shocked clasts, especially gneiss, at "Anomaly Hill" near the center of the structure (Osinski, Lee, Spray et al., 2005). We identify some gypsum clasts within samples from our westernmost outcrop, expanding the range of evaporite clasts westward, though we cannot comment on the abundance of gypsum without outcrop-scale measurements. Definitive conclusions about the presence/absence of large-scale spatial patterns of what ends up where within the impact structure will have to await a more comprehensive field data acquisition. Nevertheless, we do observe clear, quantitative compositional differences from outcrop to outcrop that relate to the underlying stratigraphy.

5.2. Implications for Understanding Impact Processes

The target rocks into which the Haughton structure formed are dominantly sedimentary, but the structure did excavate some of the basement metamorphic rocks (Osinski, Lee, Spray et al., 2005). The presence of volatiles within sedimentary targets changes the nature of melt rock when compared with melt sheets from crystalline targets (Kieffer & Simonds, 1980; Osinski et al., 2007, 2008). In particular, the enthalpies of sedimentary clasts differ from crystalline clasts, and, as a result, sedimentary clasts quench melts faster, resulting in less clast assimilation and higher overall clast content of the solidified melt rock (Cintala & Grieve, 1992; Kieffer & Simonds, 1980; Osinski et al., 2007, 2008). Whereas impact melts from crystalline targets crystallize to form silicate melt phases such as plagioclase and pyroxene, the variable nature of sedimentary rocks (e.g., carbonates vs. evaporites vs. clastic sedimentary rocks) often means that their melts can have such different physical properties that they do not mix and homogenize, instead forming particulate matrices with evidence for immiscibility (e.g., Osinski et al., 2007, 2008, 2018).

We conclude that crater-fill impact melt deposits are not homogenized within moderately sized structures formed in sedimentary rocks such as at Haughton and that heterogeneity may be the norm, not the exception. Our result is consistent with previous work at this and other impact structures (e.g., Hörz et al., 2002; Osinski et al., 2008; Osinski, Lee, Spray et al., 2005; Osinski & Spray, 2003; Siegert & Hecht, 2018), but this is the first time the heterogeneities of both clasts and groundmass have been quantified at the macroscale, and they are 10s of percentage differences. Furthermore, the compositions that we derive (Tables A1 and A2) can be used to constrain numerical models of impact structure and melt formation and emplacement for the Haughton impact structure. Numerical models must be able to explain order of magnitude differences in clast content and the presence of clasts of certain lithologies in some outcrops and near total absence in other outcrops.

Because melt heterogeneities have been observed at impact structures formed in crystalline target rocks, including Mistastin (Marion & Sylvester, 2010) and on the Moon (Dhingra et al., 2013), our results may extend to crystalline targets. While simple vertical stratigraphies such as that at Haughton are unlikely in a crystalline target, there can be subsurface heterogeneities due to magma evolution, dikes, sills, and more that could remain unhomogenized during formation of impact melt rock. Subsurface igneous compositions not nominally present at the surface could therefore be identified within the impact melt, shedding light on the composition of the subsurface.

The scale of heterogeneity observed and the types of outcrops analyzed here provide new constraints on the movement of melt during initial stages of crater formation. Dhingra et al. (2013) interpreted the spatial relations of a compositionally distinct lunar melt feature viewed from orbit as evidence for incomplete mixing of a heterogeneous target and suggested that the compositionally distinct melt was isolated initially and then drained back into the crater. Similarly, the melt rock at Haughton appears to sample different depths of a heterogeneous target rock. However, we need not invoke a mechanism for segregation of a pool of melt; instead, the Haughton emplacement processes precluded significant lateral mixing, and the melt itself quenched rapidly (e.g., Cintala & Grieve, 1992; Kieffer & Simonds, 1980; Osinski et al., 2007, 2008). The idea of intense mixing of the melt with clasts (e.g., Simonds & Kieffer, 1993), persisting in the literature as assumptions of strong convection and homogenization, did not occur at Haughton. Furthermore, there

was no homogenized melt that infiltrated and scoured deeper clasts; at Haughton, the groundmass differs by outcrop as well as the clast composition (section 5.1.2).

5.3. Implications for Planetary Studies

The scale of compositional differences observed at Haughton—contiguous outcrops up to 10s or 100s of meters horizontally that differ in composition from outcrops kilometers away—would be observable by spectrometers currently or previously orbiting other solar system bodies, including the Compact Reconnaissance Imaging Spectrometer for Mars (CRISM) on the Mars Reconnaissance Orbiter (Murchie et al., 2007), the Moon Mineralogy Mapper (M^3) on Chandrayaan-1 (Green et al., 2011; Pieters et al., 2009), and the Visible and Infrared (VIR) spectrometer on the Dawn spacecraft at Vesta and Ceres (de Sanctis, Ammannito et al., 2012; de Sanctis, Combe et al., 2012). In particular, melt derived from impacts into volatile-bearing crust on Mars (e.g., Boyce et al., 2012; Pope et al., 2006; Tornabene et al., 2012) and Ceres would be expected to be heterogeneous, as at Haughton, and identification of the different compositional units could shed light on crustal compositional variation with depth. This could illuminate the geologic history of the region beyond what is exposed outside of craters. Further analysis of such units with remote sensing data sets is warranted. While thick sedimentary sequences as at Haughton may be uncommon, igneous processes and/or differences in alteration due to temperature, pressure, fluid chemistry, and protolith may lead to spatial differences in mineral assemblages with depth. Existing spectral libraries and processing pipelines for planetary imaging spectroscopy data correct images to reflectance and standardize for observation and illumination geometries (e.g., Kokaly et al., 2017; Murchie et al., 2007), and the vast literature connecting absorption features in VSWIR spectra with mineral compositions would permit identification of heterogeneities from subsurface lithologies beyond the compositions present at Haughton.

When considering impact structures and melt sheets for landing sites in planetary exploration, the results of this study suggest that different locations within melt sheets likely sampled different subsurface materials. Primary heterogeneities could be exacerbated in the case of later reaction with fluids, which could result in different secondary mineral assemblages. In both cases, assessing these differences would be critical to selecting the best landing site for a future mission.

Finally, this study also provides an argument for collecting multiple samples of impact melt rock at different locations within a crater, particularly in sedimentary or volatile-bearing targets, in planetary sample return. A single sample of Isidis basin impact melt collected by the Mars 2020 rover and returned to Earth for analysis would likely not provide a clear picture of the entire melt body in question; multiple samples, along with in situ measurements of outcrops by the rover, would be needed to understand the subsurface lithologies represented at the surface in impactites.

6. Conclusion

Impact structures are our primary windows into the subsurface compositions of planetary bodies. This study of the impact melt rock at the 23-km diameter Haughton structure shows major compositional heterogeneities from outcrop to outcrop of clast-rich impact melt rock. The representation of target lithologies in clasts varies by >40% by area for some lithologies at outcrops within the structure separated by a few kilometers, and similar magnitudes of variation are seen in the composition of the groundmass. Furthermore, the quantitative lithologic differences in the groundmass and clasts are correlated and can be traced to specific depths of origin in the target stratigraphy. Abundances of gneiss, sandstone, and phyllosilicates show that some outcrops source materials from >1.3-km depth while others do not. Silicates are inversely proportional to abundances of shallower gypsum-bearing beds (0.9–1.1 km). The results of this work shed light on the processes of impact structure formation, and melt rock emplacement, particularly for sedimentary or volatile-bearing targets, including Mars and Ceres, but likely extend to crystalline targets on the Moon and elsewhere. For sedimentary or volatile silicate targets, we expect that the melt rock is heterogeneous, as observed at Haughton crater. The most likely explanation for the heterogeneities is that the cold clasts within the melt sheet rapidly cooled the melt sheet. Finally, this paper provides quantitative constraints for numerical models of impact crater formation that must explain this degree of heterogeneity and mixing of excavated materials.

Appendix A

Table A1
Composition of Outcrops Derived from Imaging Spectroscopy

Site	Cal	Dol	Si-OH	Gp	Ilt	Ilt-like	Carb + Si-OH	Gp + Cal	Gp + Dol	Si-OH + Gp	Unclassified[a]
Approx. source depth (km)	0.5–1.9	0–1.9	>1.3	0.9–1.1	1.6–1.7	1.6–1.7		0.5–1.9	<1.9	>0.9	
Rhinoceros Creek	31.2	7.2	9.2	0.1	0.3	8.0	41.6	0.0	0.0	0.0	5.0
South of camp	8.2	43.7	0.7	10.2	0.0	0.0	9.0	0.4	22.7	0.1	5.1
Pinnacle	39.5	1.5	0.2	2.3	0.0	0.0	1.7	36.5	18.3	0.1	0.0

Note. Areal abundances of each lithology are determined via analysis of images of outcrops. Source depths are from Osinski, Lee, Spray et al. (2005) and Osinski, Spray, and Lee (2005). Abbreviations of lithologies are Cal = calcite, Dol = dolomite, Si-OH = hydrated silica, Gp = gypsum, Ilt = illite, Ilt-like = illite-like, Carb + Si-OH = carbonate + hydrated silica, Gp + Cal = gypsum + calcite, Si-OH + Gp = hydrated silica + gypsum.
[a]Includes unknown lithologies with a 2.32 μm absorption.

Table A2
Compositions of Laboratory Samples Derived from Imaging Spectroscopy

Site	Sample	Cal	Dol	Si-OH	Gp	Ilt	Ilt-like	Carb + Si-OH	Gp + Cal	Gp + Dol	Si-OH + Gp	Unclassified[a]
						Samples cut for XRF analyses						
CSOR	1_s1	58.2	15.5	0.7	0.2	1.3	4.5	12.4	3.0	3.5	0.0	0.6
CSOR	1_s2	55.2	16.6	1.3	0.4	1.6	5.4	12.4	2.7	3.4	0.0	0.9
P	Upper_s1	12.8	20.6	1.6	26.4	0.5	2.2	7.0	5.4	21.9	0.2	1.5
P	Upper_s2	31.8	13.5	1.0	20.9	0.4	1.2	4.6	6.1	19.2	0.3	1.1
P	Lower1_s1	18.6	74.2	0.1	0.0	0.1	0.7	2.4	1.6	2.0	0.0	0.3
P	Lower1_s2	18.5	75.1	0.1	0.0	0.1	0.6	2.1	1.4	1.9	0.0	0.2
P	Lower2_s1	53.0	35.4	0.2	0.1	0.1	1.6	3.6	3.7	1.9	0.0	0.4
P	Lower2_s2	71.9	18.1	0.1	0.0	0.2	1.2	4.0	3.1	0.9	0.0	0.3
RC	Large_s1	7.2	23.5	8.5	2.9	2.6	13.2	27.4	2.1	9.8	0.1	2.6
RC	Large_s2	9.0	24.5	9.9	3.6	2.3	11.2	21.9	2.2	8.1	0.1	7.8
RC	Small_s1	23.9	19.3	4.7	2.1	3.1	10.6	23.5	3.6	7.9	0.1	1.1
RC	Small_s2	27.8	21.4	5.9	2.1	2.3	6.7	19.2	4.2	5.0	0.0	5.5
						Hand samples (breccia-type)						
CSOR	B1_1	1.2	11.8	2.7	43.4	0.3	4.6	13.3	1.2	20.8	0.0	0.8
CSOR	B2_1	7.4	43.5	1.9	8.0	2.3	6.8	18.4	1.0	7.6	0.0	3.1
CSOR	B3_1	14.7	50.0	1.8	0.5	2.5	6.4	17.5	1.0	2.8	0.0	3.0
CSOR	B4_1	5.4	31.9	2.0	0.6	3.9	12.1	36.9	0.8	5.5	0.0	1.0
CSOR	B5_1	2.5	59.6	2.0	2.6	0.4	3.8	14.1	0.5	12.2	0.0	2.2
CSOR	B6_1	0.1	23.8	1.0	42.8	0.2	3.8	13.9	3.3	10.0	0.0	1.0
CSOR	B6_2	3.9	41.7	3.1	6.2	0.2	7.3	27.2	0.5	8.8	0.0	1.2
CSOR	B6_3	34.9	25.8	0.0	1.2	0.0	0.0	0.9	3.0	34.2	0.0	0.1
WP34	B4_1	6.6	56.7	6.2	2.2	1.0	5.5	12.4	0.4	4.5	0.0	4.6
WP34	B4_2	1.1	22.3	3.1	45.7	0.8	3.6	10.6	0.6	10.2	0.0	2.1
WP34	B4_3	6.7	51.1	2.2	3.6	1.7	4.9	19.7	0.6	6.2	0.0	3.3
OSOR	B1_1	0.4	2.1	0.5	83.5	0.4	0.4	1.0	0.6	10.4	0.1	0.7
OSOR	B2_1	3.5	13.2	0.2	58.8	0.1	0.3	0.9	1.9	20.2	0.1	0.8
OSOR	B3_1	8.4	8.4	0.0	46.1	0.0	0.3	0.2	1.8	34.5	0.0	0.2
OSOR	B3_2	0.0	0.2	0.3	97.8	0.1	0.2	0.1	0.0	1.4	0.0	0.1
OSOR	B3_3	0.5	0.8	0.2	95.4	0.0	0.1	0.1	0.5	1.9	0.4	0.3
P	B_lower1_1	39.5	55.8	0.0	0.0	0.0	1.0	0.9	1.0	1.5	0.0	0.2
P	B_lower2_1	26.8	41.1	0.1	24.1	0.0	0.4	0.6	2.0	4.6	0.0	0.2
P	B_lower2_2	79.0	19.3	0.0	0.0	0.0	0.2	0.0	1.0	0.5	0.0	0.0
P	B_upper1_1	9.3	38.1	0.5	19.7	0.3	2.4	5.6	3.0	20.3	0.4	0.3
P	B_upper2_1	3.0	18.0	0.5	53.4	0.5	1.2	1.4	2.0	19.5	0.0	0.3
P	B_upper2_2	3.5	13.1	0.5	55.3	0.6	2.7	1.4	1.7	20.3	0.0	1.0
P	B_upper2_3	7.2	22.9	0.1	42.1	0.0	1.1	2.1	1.3	23.1	0.0	0.1
RC	B1	7.7	29.7	1.3	0.3	3.7	12.4	42.6	0.3	2.0	0.0	0.0
RC	B2	11.1	37.0	1.8	0.4	1.7	12.5	31.4	0.3	3.3	0.0	0.5
RC	B3	9.3	27.3	3.1	1.5	2.7	12.9	27.9	2.5	10.9	0.0	2.0

Table A2
Continued

Site	Sample	Cal	Dol	Si-OH	Gp	Ilt	Ilt-like	Carb + Si-OH	Gp + Cal	Gp + Dol	Si-OH + Gp	Unclassified[a]
RC	B3_s2	6.8	21.7	5.0	3.1	3.9	11.0	27.4	2.8	15.8	0.0	2.4
SOC	B1_1	5.5	18.7	2.4	27.6	0.1	2.5	7.2	2.6	29.4	0.2	3.8
SOC	B1_2	1.0	9.7	1.1	54.6	0.1	0.7	2.5	1.1	27.3	0.0	1.9
SOC	B1_3	7.6	11.0	1.3	49.7	0.1	0.9	3.2	2.8	20.9	0.0	2.5
SOC	B1_4	0.2	13.3	6.3	48.8	0.6	2.2	4.0	0.1	14.3	0.0	10.4
SOC	B1_5	0.5	6.8	2.2	66.4	0.2	0.2	1.6	0.3	15.7	0.0	6.1
SOC	B1_6	6.6	33.9	0.9	13.3	0.2	4.0	8.1	0.8	29.8	0.0	2.5
SOC	B1_7	1.8	21.2	1.6	42.0	0.2	1.6	4.2	0.6	22.7	0.0	4.0
SOC	B1_8	1.1	3.3	2.7	79.7	0.1	0.4	1.2	0.4	5.6	0.0	5.6
SOC	B1_9	2.6	27.7	1.9	30.1	0.3	2.6	6.3	0.8	23.1	0.0	4.6
SOC	B1_10	1.0	15.4	1.4	40.3	0.1	0.9	4.0	0.5	32.0	0.0	4.3
SOC	B2	3.8	15.0	0.0	37.6	0.0	0.4	0.4	0.4	41.5	0.0	0.9
						Clasts and cobbles						
OSOR	C1_1	0.0	0.0	91.6	7.6	0.0	0.0	0.0	0.0	0.0	0.1	0.3
OSOR	C1_2	0.0	0.0	11.7	87.2	0.2	0.0	0.0	0.0	0.0	0.5	0.2
OSOR	C1_3	0.1	0.6	73.4	22.6	0.0	0.0	0.1	0.0	0.0	0.2	1.4
OSOR	C1_5	0.1	0.1	87.1	10.5	0.2	0.1	0.3	0.0	0.1	0.0	1.4
RC	C1_1	0.0	0.1	93.2	1.6	0.0	0.4	4.2	0.0	0.0	0.0	0.5
RC	C1_3	97.7	0.1	0.0	0.0	0.0	0.1	0.6	1.5	0.0	0.0	0.0
RC	C1_4	97.8	0.9	0.0	0.0	0.1	0.1	0.8	0.1	0.0	0.0	0.3
RC	C1_5	1.8	89.4	0.6	0.1	0.0	0.2	5.4	0.0	2.4	0.0	0.1
RC	C2_2	91.4	0.6	0.0	0.2	0.0	0.1	0.3	5.9	0.1	0.0	1.3
RC	C2_3	97.1	0.1	0.0	0.0	0.0	0.0	0.3	2.5	0.0	0.0	0.0
RC	C3_1	92.4	0.1	0.2	0.1	0.9	0.2	3.6	2.4	0.0	0.0	0.3
RC	C3_2	70.1	24.2	0.0	0.1	0.0	0.3	0.3	2.7	1.6	0.0	0.6
RC	C3_3	0.0	0.0	61.4	0.9	31.8	5.8	0.1	0.0	0.0	0.0	0.1
RC	C3_4	99.1	0.8	0.0	0.0	0.0	0.0	0.0	0.1	0.0	0.0	0.0
RC	C3_5	90.6	0.1	0.0	0.0	0.0	0.2	0.8	8.3	0.0	0.0	0.0
RC	C3_6	0.0	0.0	91.6	6.4	0.0	0.0	1.9	0.0	0.0	0.0	0.0
RC	C3_7	98.1	1.8	0.0	0.0	0.0	0.0	0.0	0.1	0.0	0.0	0.1
RC	C4_1	0.0	0.0	63.5	31.6	1.6	2.3	0.6	0.0	0.0	0.1	0.2
RC	C5_1	13.9	3.9	11.2	7.8	3.6	20.1	1.4	0.9	0.6	0.0	36.6
RC	C5_2	0.0	0.0	85.4	2.8	0.1	0.3	0.2	0.0	0.0	0.0	11.5
RC	C5_4	0.1	0.2	69.7	24.4	0.5	2.5	0.6	0.0	0.1	0.0	1.9
RC	C5_5	85.5	0.0	0.3	0.0	1.9	0.5	8.1	3.5	0.0	0.0	0.1
RC	C6_1	8.3	10.5	6.9	0.2	0.8	60.7	9.5	0.6	0.5	0.0	2.3
RC	C6_2	6.6	42.1	11.1	0.7	0.2	23.7	12.0	0.2	0.6	0.0	2.8
RC	C6_3	7.6	24.0	2.7	0.3	0.3	46.3	14.0	0.4	0.5	0.0	3.9
RC	C6_4	3.5	7.3	10.8	20.0	2.3	45.9	5.8	0.7	2.6	0.0	1.1
RC	C7_1	1.9	45.8	7.4	10.0	0.6	11.7	5.3	0.2	4.3	0.0	12.9
SOC	C1_1	0.0	0.0	0.0	99.8	0.0	0.0	0.0	0.0	0.0	0.0	0.1
SOC	C1_2	97.5	0.1	0.0	0.0	0.0	0.0	0.0	2.3	0.0	0.0	0.0
SOC	C1_3	0.0	0.0	0.0	99.6	0.0	0.0	0.0	0.0	0.3	0.0	0.0
SOC	C1_4	15.1	67.4	0.0	2.8	0.0	0.0	0.1	2.8	11.8	0.0	0.1
SOC	C1_5	0.0	27.9	6.5	23.6	0.0	0.8	5.3	0.0	7.2	0.0	28.7
SOC	C1_6	0.0	91.1	0.0	0.7	0.0	0.0	0.0	0.0	8.1	0.0	0.0
SOC	C2_1	0.2	77.9	0.0	0.7	0.0	0.0	0.0	0.0	21.2	0.0	0.1
SOC	C2_2	0.1	0.6	46.3	21.2	0.4	2.4	0.9	0.0	0.4	0.0	27.7
SOC	C3_1	0.0	88.2	0.0	2.8	0.0	0.0	0.1	0.0	8.9	0.0	0.0
SOC	C3_2	0.0	93.6	0.0	1.1	0.0	0.0	0.0	0.0	5.2	0.0	0.0
SOC	C3_3	0.0	0.0	0.0	99.9	0.0	0.0	0.0	0.0	0.1	0.0	0.1
SOC	C3_4	95.8	0.0	0.0	1.6	0.0	0.0	0.0	2.1	0.4	0.0	0.0
SOC	C3_5	94.7	1.3	0.0	0.1	0.0	0.0	0.0	3.8	0.0	0.0	0.0
SOC	C3_6	0.0	0.1	0.0	98.1	0.0	0.0	0.0	0.2	1.4	0.0	0.1

Note. All values are in areal percentage abundances. Locations are Creek South of Rhinoceros Creek (CSOR), Overhang south of Rhinoceros Creek (OSOR), Pinnacle (P), Rhinoceros Creek (RC), South of Camp (SOC), and Western outcrop/Waypoint 34 (WP34). Abbreviations of lithologies are Cal = calcite, Dol = dolomite, Si-OH = hydrated silica, Gp = gypsum, Ilt = illite, Ilt-like = illite-like, Carb + Si-OH = carbonate + hydrated silica, Gp + Cal = gypsum + calcite, Si-OH + Gp = hydrated silica + gypsum.
[a]Includes unknown lithologies with a 2.32-μm absorption.

Data Availability Statement

Imaging spectroscopy and XRF data sets for this research are available at the Zenodo repository (Greenberger et al., 2020): https://doi.org/10.5281/zenodo.3470194.

Acknowledgments

We gratefully acknowledge the other members of the field team (Chris Carr, Byung-Hun Choe, Shamus Duff, Etienne Godin, Anna Grau, Elise Harrington, Mark Jellinek, Anterro Kukko, Catherine Neish, Jen Newman, Alex Pontefract, and Mike Zanetti), especially for packing up camp to allow us to image two last sites, while twin otters were en route during a sudden early pullout on the first cloudless day and for giving us ATV's whenever the sun showed signs of coming out. We thank Aaron Celestian at the Los Angeles Natural History Museum for assistance in acquiring XRF data. We also are grateful to the Polar Continental Shelf Program for logistical support. RNG was supported by a NASA Postdoctoral Program Fellowship, administered by Universities Space Research Association, with an appointment at the Jet Propulsion Laboratory, California Institute of Technology, and also thanks a grant from the Barringer Family Fund for Meteorite Impact Research for contributing toward travel costs. BLE acknowledges support from the Rose Hills Foundation and a NASA Planetary Major Equipment grant (NNX13AG74G). GRO acknowledges support from the Natural Sciences and Engineering Research Council of Canada's Discovery Grant and Northern Research Supplement programs. We thank Patrick Pinet, four anonymous reviewers, and Editor David Baratoux for their helpful comments that improved this paper.

References

Adams, J. B., Sabol, D. E., Kapos, V., Almeida Filho, R., Roberts, D. A., Smith, M. O., & Gillespie, A. R. (1995). Classification of multispectral images based on fractions of endmembers: Application to land-cover change in the Brazilian Amazon. *Remote Sensing of Environment*, *52*(2), 137–154. https://doi.org/10.1016/0034-4257(94)00098-8

Adams, J. B., Smith, M. O., & Johnson, P. E. (1986). Spectral mixture modeling: A new analysis of rock and soil types at the Viking Lander 1 site. *Journal of Geophysical Research*, *91*(B8), 8098–8112. https://doi.org/10.1029/JB091iB08p08098

Aines, R. D., & Rossman, G. R. (1984). Water in minerals? A peak in the infrared. *Journal of Geophysical Research*, *89*(B6), 4059–4071. https://doi.org/10.1029/JB089iB06p04059

Anderson, J. H., & Wickersheim, K. A. (1964). Near infrared characterization of water and hydroxyl groups on silica surfaces. *Surface Science*, *2*, 252–260. https://doi.org/10.1016/0039-6028(64)90064-0

Arvidson, R. E., Squyres, S. W., Bell, J. F., Catalano, J. G., Clark, B. C., Crumpler, L. S., et al. (2014). Ancient Aqueous Environments at Endeavour Crater, Mars. *Science*, *343*(6169), 1,248,097. https://doi.org/10.1126/science.1248097

Bibring, J.-P., Langevin, Y., Gendrin, A., Gondet, B., Poulet, F., Berthé, M., et al. (2005). Mars surface diversity as revealed by the OMEGA/Mars express observations. *Science*, *307*(5715), 1576–1581. https://doi.org/10.1126/science.1108806

Bishop, J. L., Lane, M. D., Dyar, M. D., & Brown, A. J. (2008). Reflectance and emission spectroscopy study of four groups of phyllosilicates: Smectites, kaolinite-serpentines, chlorites and micas. *Clay Minerals*, *43*(1), 35–54. https://doi.org/10.1180/claymin.2008.043.1.03

Boyce, J. M., Wilson, L., Mouginis-Mark, P. J., Hamilton, C. W., & Tornabene, L. L. (2012). Origin of small pits in Martian impact craters. *Icarus*, *221*(1), 262–275. https://doi.org/10.1016/j.icarus.2012.07.027

Burns, R. G. (1993). *Mineralogical applications of crystal field theory* (2nd ed.). Cambridge: Cambridge University Press. https://doi.org/10.1017/CBO9780511524899

Cassanelli, J. P., & Head, J. W. (2016). Did the Orientale impact melt sheet undergo large-scale igneous differentiation by crystal settling? *Geophysical Research Letters*, *43*, 11,156–11,165. https://doi.org/10.1002/2016GL070425

Chavez Jr., P. S. (1988). An improved dark-object subtraction technique for atmospheric scattering correction of multispectral data. *Remote Sensing of Environment*, *24*(3), 459–479. https://doi.org/10.1016/0034-4257(88)90019-3

Chavez, P. S. Jr. (1996). Image-based atmospheric corrections-revisited and improved. *Photogrammetric Engineering & Remote Sensing*, *62*(9), 1025–1036.

Cintala, M. J., & Grieve, R. A. F. (1992). The effects of differential scaling of impact melt and crater dimensions on lunar and terrestrial craters: Some brief examples. *Geological Society of America Special Papers*, *293*, 51–60. https://doi.org/10.1130/SPE293-p51

Clark, R. N., King, T. V. V., Klejwa, M., Swayze, G. A., & Vergo, N. (1990). High spectral resolution reflectance spectroscopy of minerals. *Journal of Geophysical Research*, *95*(B8), 12,653–12,680. https://doi.org/10.1029/JB095iB08p12653

Clark, R. N., & Roush, T. L. (1984). Reflectance spectroscopy: Quantitative analysis techniques for remote sensing applications. *Journal of Geophysical Research*, *89*(B7), 6329–6340. https://doi.org/10.1029/JB089iB07p06329

Clark, R. N., Swayze, G. A., Livo, K. E., Kokaly, R. F., Sutley, S. J., Dalton, J. B., et al. (2003). Imaging spectroscopy: Earth and planetary remote sensing with the USGS Tetracorder and expert systems. *Journal of Geophysical Research*, *108*(E12), 5131. https://doi.org/10.1029/2002JE001847

Clark, R. N., Swayze, G. A., Wise, R., Livo, E., Hoefen, T., Kokaly, R., & Sutley, S. J. (2007). USGS digital spectral library splib06a. *Reston, VA: US Geological Survey, Data Series*, *231*. https://doi.org/10.3133/ds231

Cloutis, E. A., Grasby, S. E., Last, W. M., Léveillé, R., Osinski, G. R., & Sherriff, B. L. (2010). Spectral reflectance properties of carbonates from terrestrial analogue environments: Implications for Mars. *Planetary and Space Science*, *58*(4), 522–537. https://doi.org/10.1016/j.pss.2009.09.002

Cloutis, E. A., Hawthorne, F. C., Mertzman, S. A., Krenn, K., Craig, M. A., Marcino, D., et al. (2006). Detection and discrimination of sulfate minerals using reflectance spectroscopy. *Icarus*, *184*(1), 121–157. https://doi.org/10.1016/j.icarus.2006.04.003

Crowley, J. K., Hubbard, B. E., & Mars, J. C. (2003). Analysis of potential debris flow source areas on Mount Shasta, California, by using airborne and satellite remote sensing data. *Remote Sensing of Environment*, *87*(2–3), 345–358. https://doi.org/10.1016/j.rse.2003.08.003

de Sanctis, M. C., Ammannito, E., Capria, M. T., Tosi, F., Capaccioni, F., Zambon, F., et al. (2012). Spectroscopic characterization of mineralogy and its diversity across Vesta. *Science*, *336*(6082), 697–700. https://doi.org/10.1126/science.1219270

de Sanctis, M. C., Combe, J.-P., Ammannito, E., Palomba, E., Longobardo, A., McCord, T. B., et al. (2012). Detection of widespread hydrated materials on Vesta by the VIR imaging spectrometer on board the Dawn Mission. *The Astrophysical Journal Letters*, *758*(2), L36. https://doi.org/10.1088/2041-8205/758/2/L36

Dence, M. R. (1971). Impact melts. *Journal of Geophysical Research*, *76*(23), 5552–5565. https://doi.org/10.1029/JB076i023p05552

Dhingra, D., Pieters, C. M., Head, J. W., & Isaacson, P. J. (2013). Large mineralogically distinct impact melt feature at Copernicus crater—Evidence for retention of compositional heterogeneity. *Geophysical Research Letters*, *40*(6), 1043–1048. https://doi.org/10.1002/grl.50255

Dressler, B. O., & Reimold, W. U. (2001). Terrestrial impact melt rocks and glasses. *Earth-Science Reviews*, *56*(1–4), 205–284. https://doi.org/10.1016/S0012-8252(01)00064-2

Ehlmann, B. L., Mustard, J. F., Swayze, G. A., Clark, R. N., Bishop, J. L., Poulet, F., et al. (2009). Identification of hydrated silicate minerals on Mars using MRO-CRISM: Geologic context near Nili Fossae and implications for aqueous alteration. *Journal of Geophysical Research*, *114*, E00D08. https://doi.org/10.1029/2009JE003339

Flemming, R. L., Newman, J. D., Botor, R. J., Cao, F., Caudill, C. M., Galarneau, M. R., et al. (2018). Preliminary investigation of shocked carbonates from the haughton impact structure, Devon Island, NU, using X-ray diffraction and rietveld refinement (Vol. *49*, p. 3000). Presented at the Lunar and Planetary Science Conference, The Woodlands, TX.

Floran, R. J., Grieve, R. A. F., Phinney, W. C., Warner, J. L., Simonds, C. H., Blanchard, D. P., & Dence, M. R. (1978). Manicouagan impact melt, Quebec, 1, stratigraphy, petrology, and chemistry. *Journal of Geophysical Research*, *83*(B6), 2737–2759. https://doi.org/10.1029/JB083iB06p02737

Floran, R. J., Simonds, C. H., Grieve, R. a. F., Phinney, W. C., Warner, J. L., Rhodes, M. J., et al. (1976). Petrology, structure and origin of the Manicouagan melt sheet, Quebec, Canada: A preliminary report Floran ET AL. *Geophysical Research Letters*, *3*(2), 49–52. https://doi.org/10.1029/GL003i002p00049

Friedlander, L. R., Glotch, T. D., Bish, D. L., Dyar, M. D., Sharp, T. G., Sklute, E. C., & Michalski, J. R. (2015). Structural and spectroscopic changes to natural nontronite induced by experimental impacts between 10 and 40 GPa. *Journal of Geophysical Research: Planets*, *120*, 888–912. https://doi.org/10.1002/2014JE004638

Friedlander, L. R., Glotch, T. D., Phillips, B. L., Vaughn, J. S., & Michalski, J. R. (2016). Examining structural and related spectral change in Mars-relevant phyllosilicates after experimental impacts between 10 and 40 Gpa. *Clays and Clay Minerals*, *64*(3), 189–209. https://doi.org/10.1346/CCMN.2016.0640302

Frisch, T., & Thorsteinsson, R. (1978). Haughton Astrobleme: A Mid-Cenozoic impact crater Devon Island, Canadian Arctic Archipelago. *Arctic*, *31*(2), 108–124.

Gaffey, S. J. (1985). Reflectance spectroscopy in the visible and near-infrared (0.35–2.55 μm): Applications in carbonate petrology. *Geology*, *13*(4), 270–273. https://doi.org/10.1130/0091-7613(1985)13<270:RSITVA>2.0.CO;2

Gaffey, S. J. (1986). Spectral reflectance of carbonate minerals in the visible and near infrared (0.35–2.55 microns); calcite, aragonite, and dolomite. *American Mineralogist*, *71*(1–2), 151–162.

Gaffey, S. J. (1987). Spectral reflectance of carbonate minerals in the visible and near infrared (0.35–2.55 um): Anhydrous carbonate minerals. *Journal of Geophysical Research*, *92*(B2), 1429–1440. https://doi.org/10.1029/JB092iB02p01429

Goetz, A. F. H., Vane, G., Solomon, J. E., & Rock, B. N. (1985). Imaging spectrometry for earth remote sensing. *Science*, *228*(4704), 1147–1153. https://doi.org/10.1126/science.228.4704.1147

Goryniuk, M. C., Rivard, B. A., & Jones, B. (2004). The reflectance spectra of opal-A (0.5–25 μm) from the Taupo Volcanic Zone: Spectra that may identify hydrothermal systems on planetary surfaces. *Geophysical Research Letters*, *31*, L24701. https://doi.org/10.1029/2004GL021481

Green, R. O., Pieters, C., Mouroulis, P., Eastwood, M., Boardman, J., Glavich, T., et al. (2011). The Moon Mineralogy Mapper (M3) imaging spectrometer for lunar science: Instrument description, calibration, on-orbit measurements, science data calibration and on-orbit validation. *Journal of Geophysical Research*, *116*, E00G19. https://doi.org/10.1029/2011JE003797

Greenberger, R. N., Ehlmann, B. L., Osinski, G. R., Tornabene, L. L., & Green, R. O. (2020). Imaging spectroscopy and elemental mapping of Haughton impact melt rock: Datasets. *Zenodo Data Repository.* https://doi.org/10.5281/zenodo.3470194

Greenberger, R. N., Mustard, J. F., Ehlmann, B. L., Blaney, D. L., Cloutis, E. A., Wilson, J. H., et al. (2015). Imaging spectroscopy of geological samples and outcrops: Novel insights from microns to meters. *GSA Today*, *25*(12), 4–10. https://doi.org/10.1130/GSATG252A.1

Greenberger, R. N., Mustard, J. F., Osinski, G. R., Tornabene, L. L., Pontefract, A. J., Marion, C. L., et al. (2016). Hyperspectral mapping of alteration assemblages within a hydrothermal vug at the Haughton impact structure, Canada. *Meteoritics & Planetary Science*, *51*(12), 2274–2292. https://doi.org/10.1111/maps.12716

Grieve, R. A. F. (1975). Petrology and chemistry of the impact melt at Mistastin Lake crater, Labrador. *Geological Society of America Bulletin*, *86*(12), 1617–1629. https://doi.org/10.1130/0016-7606(1975)86<1617:PACOTI>2.0.CO;2

Grieve, R. A. F. (1987). Terrestrial Impact Structures. *Annual Review of Earth and Planetary Sciences*, *15*(1), 245–270. https://doi.org/10.1146/annurev.ea.15.050187.001333

Grieve, R. A. F., & Cintala, M. J. (1997). Planetary differences in impact melting. *Advances in Space Research*, *20*(8), 1551–1560. https://doi.org/10.1016/S0273-1177(97)00877-6

Grieve, R. A. F., Dence, M. R., & Robertson, P. B. (1977). Cratering processes—As interpreted from the occurrence of impact melts. In D. J. Roddy, R. O. Pepin, & R. B. Merrill (Eds.), *Impact and explosion cratering* (pp. 791–814). New York: Pergamon Press.

Hapke, B. (1981). Bidirectional reflectance spectroscopy: 1. Theory. *Journal of Geophysical Research*, *86*(B4), 3039–3054. https://doi.org/10.1029/JB086iB04p03039

Hörz, F., Mittlefehldt, D. W., See, T. H., & Galindo, C. (2002). Petrographic studies of the impact melts from Meteor Crater, Arizona, USA. *Meteoritics & Planetary Science*, *37*(4), 501–531. https://doi.org/10.1111/j.1945-5100.2002.tb00836.x

Hunt, G. R., & Salisbury, J. W. (1971). Visible and near infrared spectra of minerals and rocks. II. Carbonates. *Modern Geology*, *2*, 23–30.

Hunt, G. R., Salisbury, J. W., & Lenhoff, C. J. (1971). Visible and near-infrared spectra of minerals and rocks: IV. Sulphides and sulphates. *Mod. Geol*, *3*, 1–14.

Izawa, M. R. M., Cloutis, E. A., Rhind, T., Mertzman, S. A., Poitras, J., Applin, D. M., & Mann, P. (2018). Spectral reflectance (0.35–2.5 μm) properties of garnets: Implications for remote sensing detection and characterization. *Icarus, 300* (Supplement C, 392–410. https://doi.org/10.1016/j.icarus.2017.09.005

Kieffer, S. W., & Simonds, C. H. (1980). The role of volatiles and lithology in the impact cratering process. *Reviews of Geophysics*, *18*(1), 143–181. https://doi.org/10.1029/RG018i001p00143

Koeberl, C., Claeys, P., Hecht, L., & McDonald, I. (2012). Geochemistry of impactites. *Elements*, *8*(1), 37–42. https://doi.org/10.2113/gselements.8.1.37

Kokaly, R. F., Clark, R. N., Swayze, G. A., Livo, K. E., Hoefen, T. M., Pearson, N. C., et al. (2017). USGS Spectral Library Version 7. Reston, VA: *U.S. Geological Survey Data Series 1035*, 61 p. https://doi.org/10.3133/ds1035

Marion, C. L., & Sylvester, P. J. (2010). Composition and heterogeneity of anorthositic impact melt at Mistastin Lake crater, Labrador. *Planetary and Space Science*, *58*(4), 552–573. https://doi.org/10.1016/j.pss.2009.09.018

Murchie, S., Arvidson, R., Bedini, P., Beisser, K., Bibring, J.-P., Bishop, J., et al. (2007). Compact Reconnaissance Imaging Spectrometer for Mars (CRISM) on Mars Reconnaissance Orbiter (MRO). *Journal of Geophysical Research*, *112*, 57. https://doi.org/10.1029/2006JE002682

Mustard, J. F., Murchie, S. L., Pelkey, S. M., Ehlmann, B. L., Milliken, R. E., Grant, J. A., et al. (2008). Hydrated silicate minerals on Mars observed by the Mars reconnaissance Orbiter CRISM instrument. *Nature*, *454*(7202), 305–309. https://doi.org/10.1038/nature07097

Muttik, N., Kirsimäe, K., Somelar, P., & Osinski, G. R. (2008). Post-impact alteration of surficial suevites in Ries crater, Germany: Hydrothermal modification or weathering processes? *Meteoritics & Planetary Science*, *43*(11), 1827–1840. https://doi.org/10.1111/j.1945-5100.2008.tb00646.x

Muttik, N., Kirsimäe, K., & Vennemann, T. W. (2010). Stable isotope composition of smectite in suevites at the Ries crater, Germany: Implications for hydrous alteration of impactites. *Earth and Planetary Science Letters*, *299*(1–2), 190–195. https://doi.org/10.1016/j.epsl.2010.08.034

Neish, C. D., Madden, J., Carter, L. M., Hawke, B. R., Giguere, T., Bray, V. J., et al. (2014). Global distribution of lunar impact melt flows. *Icarus*, *239*, 105–117. https://doi.org/10.1016/j.icarus.2014.05.049

Newsom, H. E., Graup, G., Sewards, T., & Keil, K. (1986). Fluidization and hydrothermal alteration of the Suevite deposit at the Ries crater, West Germany, and implications for Mars. *Journal of Geophysical Research*, *91*(B13), E239–E251. https://doi.org/10.1029/JB091iB13p0E239

O'Connell-Cooper, C. D., & Spray, J. G. (2011). Geochemistry of the impact-generated melt sheet at Manicouagan: Evidence for fractional crystallization. *Journal of Geophysical Research*, *116*, B06204. https://doi.org/10.1029/2010JB008084

Öhman, T., Kramer, G. Y., & Kring, D. A. (2014). Characterization of melt and ejecta deposits of Kepler crater from remote sensing data. *Journal of Geophysical Research*, *116*, 1238–1258. https://doi.org/10.1002/2013JE004501

Osinski, G. R. (2005). Hydrothermal activity associated with the Ries impact event, Germany. *Geofluids*, *5*(3), 202–220. https://doi.org/10.1111/j.1468-8123.2005.00119.x

Osinski, G. R., Grieve, R. A. F., Collins, G. S., Marion, C., & Sylvester, P. (2008). The effect of target lithology on the products of impact melting. *Meteoritics & Planetary Science*, *43*(12), 1939–1954. https://doi.org/10.1111/j.1945-5100.2008.tb00654.x

Osinski, G. R., Grieve, R. A. F., Bleacher, J. E., Neish, C. D., Pilles, E. A., & Tornabene, L. L. (2018). Igneous rocks formed by hypervelocity impact. *Journal of Volcanology and Geothermal Research*, *353*, 25–54. https://doi.org/10.1016/j.jvolgeores.2018.01.015

Osinski, G. R., Lee, P., Parnell, J., Spray, J. G., & Baron, M. (2005). A case study of impact-induced hydrothermal activity: The Haughton impact structure, Devon Island, Canadian High Arctic. *Meteoritics & Planetary Science*, *40*(12), 1859–1877. https://doi.org/10.1111/j.1945-5100.2005.tb00150.x

Osinski, G. R., Lee, P., Spray, J. G., Parnell, J., Lim, D. S. S., Bunch, T. E., et al. (2005). Geological overview and cratering model for the Haughton impact structure, Devon Island, Canadian High Arctic. *Meteoritics & Planetary Science*, *40*(12), 1759–1776. https://doi.org/10.1111/j.1945-5100.2005.tb00145.x

Osinski, G. R., & Spray, J. G. (2001). Impact-generated carbonate melts: Evidence from the Haughton structure, Canada. *Earth and Planetary Science Letters*, *194*(1–2), 17–29. https://doi.org/10.1016/S0012-821X(01)00558-1

Osinski, G. R., & Spray, J. G. (2003). Evidence for the shock melting of sulfates from the Haughton impact structure, Arctic Canada. *Earth and Planetary Science Letters*, *215*(3–4), 357–370. https://doi.org/10.1016/S0012-821X(03)00420-5

Osinski, G. R., Spray, J. G., & Grieve, R. A. F. (2007). Impact melting in sedimentary target rocks: An assessment. In Special Paper 437: The Sedimentary Record of Meteorite Impacts (Vol. *437*, pp. 1–18). *Geological Society of America*. https://doi.org/10.1130/2008.2437(01)

Osinski, G. R., Spray, J. G., & Lee, P. (2001). Impact-induced hydrothermal activity within the Haughton impact structure, arctic Canada: Generation of a transient, warm, wet oasis. *Meteoritics & Planetary Science*, *36*(5), 731–745. https://doi.org/10.1111/j.1945-5100.2001.tb01910.x

Osinski, G. R., Spray, J. G., & Lee, P. (2005). Impactites of the Haughton impact structure, Devon Island, Canadian High Arctic. *Meteoritics & Planetary Science*, *40*(12), 1789–1812. https://doi.org/10.1111/j.1945-5100.2005.tb00147.x

Palme, H., Goebel, E., & Grieve, R. A. F. (1979). The distribution of volatile and siderophile elements in the impact melt of East Clearwater/Quebec/ (Vol. *10*, pp. 2465–2492). Presented at the *Lunar and Planetary Science Conference Proceedings*. Retrieved from http://adsabs.harvard.edu/abs/1979LPSC10.2465P

Pan, C., Rogers, A. D., & Michalski, J. R. (2015). Thermal and near-infrared analyses of central peaks of Martian impact craters: Evidence for a heterogeneous Martian crust. *Journal of Geophysical Research: Planets*, *120*. https://doi.org/10.1002/2014JE004676

Pan, L., Ehlmann, B. L., Asimow, P. D., Hu, J., & Greenberger, R. N. (2018). An infrared spectroscopy study of impact shocked carbonates and implications for Mars (Vol. *49*, p. 1896). Presented at the *Lunar and Planetary Science Conference*, The Woodlands, TX.

Pan, L., Ehlmann, B. L., Carter, J., & Ernst, C. M. (2017). The stratigraphy and history of Mars' northern lowlands through mineralogy of impact craters: A comprehensive survey. *Journal of Geophysical Research: Planets*, *122*. https://doi.org/10.1002/2017JE005276

Pelkey, S. M., Mustard, J. F., Murchie, S., Clancy, R. T., Wolff, M., Smith, M., et al. (2007). CRISM multispectral summary products: Parameterizing mineral diversity on Mars from reflectance. *Journal of Geophysical Research*, *112*, E08S14. https://doi.org/10.1029/2006JE002831

Pieters, C. M. (1986). Composition of the lunar highland crust from near-infrared spectroscopy. *Reviews of Geophysics*, *24*(3), 557–578. https://doi.org/10.1029/RG024i003p00557

Pieters, C. M., Besse, S., Boardman, J., Buratti, B., Cheek, L., Clark, R. N., et al. (2011). Mg-spinel lithology: A new rock type on the lunar farside. *Journal of Geophysical Research*, *116*, E00G08. https://doi.org/10.1029/2010JE003727

Pieters, C. M., Boardman, J., Buratti, B., Chatterjee, A., Clark, R., Glavich, T., et al. (2009). The Moon Mineralogy Mapper (M3) on Chandrayaan-1. *Current Science*, *96*(4), 500–505.

Pinet, P., Chevrel, S., & Martin, P. (1993). Copernicus: A regional probe to lunar interior. *Science*, *260*(5109), 797–801. https://doi.org/10.1126/science.260.5109.797

Pope, K. O., Kieffer, S. W., & Ames, D. E. (2006). Impact melt sheet formation on Mars and its implication for hydrothermal systems and exobiology. *Icarus*, *183*(1), 1–9. https://doi.org/10.1016/j.icarus.2006.01.012

Raikhlin, A. I., & Masaitis, V. L. (2019). Petrochemistry and geochemistry of Impactites and target crystalline rocks. In V. Masaitis (Ed.), *Popigai impact structure and its diamond-bearing rocks*, *Impact Studies* (pp. 127–135). Cham: Springer. https://doi.org/10.1007/978-3-319-77988-1_5

Redeker, H.-J., & Stöffler, D. (1988). The allochthonous polymict breccia layer of the Haughton Impact Crater, Devon Island, Canada. *Meteoritics*, *23*(3), 185–196. https://doi.org/10.1111/j.1945-5100.1988.tb01281.x

Ryder, G., & Wood, J. A. (1977). Serenitatis and imbrium impact melts—Implications for large-scale layering in the lunar crust (Vol. *8*, pp. 655–668). Presented at the *Lunar and Planetary Science Conference Proceedings*, The Woodlands, TX.

Schmitt, R.-T., Hecht, L., Stöffler, D., & Siegert, S. (2017). Geochemical data of crystalline target lithologies of the Ries impact crater. *Germany, GFZ Data Services*. https://doi.org/10.5880/fidgeo.2017.001

Siegert, S., & Hecht, L. (2018). Heterogeneity of melts in impact deposits and implications for their origin (Ries suevite, Germany). *Meteoritics & Planetary Science*, 39 pp. https://doi.org/10.1111/maps.13210

Simonds, C. H., & Kieffer, S. W. (1993). Impact and volcanism: A momentum scaling law for erosion. *Journal of Geophysical Research*, *98*(B8), 14,321–14,337. https://doi.org/10.1029/93JB00704

Singer, R. B. (1980). The dark materials on Mars: I. New information from reflectance spectroscopy on the extent and mode of oxidation. *Lunar and Planetary Science Conference*, *11*, 1045–1047.

Skála, R. (2002). Shock-induced phenomena in limestones in the quarry near Ronheim, the Ries Crater, Germany. *Bulletin of the Czech Geological Survey*, *77*(4), 313–320.

Skála, R., & Jakes, P. (1999). Shock-induced effects in natural calcite-rich targets as revealed by X-ray powder diffraction. *Special Papers-Geological Society of America*, 205–214.

Squyres, S. W., Arvidson, R. E., Bell, J. F., Calef, F., Clark, B. C., Cohen, B. A., et al. (2012). Ancient impact and aqueous processes at Endeavour Crater, Mars. *Science*, *336*(6081), 570–576. https://doi.org/10.1126/science.1220476

Squyres, S. W., Knoll, A. H., Arvidson, R. E., Ashley, J. W., Bell, J. F., Calvin, W. M., et al. (2009). Exploration of Victoria Crater by the Mars Rover Opportunity. *Science*, *324*(5930), 1058–1061. https://doi.org/10.1126/science.1170355

Sun, V. Z., & Milliken, R. E. (2015). Ancient and recent clay formation on Mars as revealed from a global survey of hydrous minerals in crater central peaks. *Journal of Geophysical Research: Planets*, *120*, 2293–2332. https://doi.org/10.1002/2015JE004918

Tornabene, L. L., Moersch, J. E., Osinski, G. R., Lee, P., & Wright, S. P. (2005). Spaceborne visible and thermal infrared lithologic mapping of impact-exposed subsurface lithologies at the Haughton impact structure, Devon Island, Canadian High Arctic: Applications to Mars. *Meteoritics & Planetary Science*, *40*(12), 1835–1858. https://doi.org/10.1111/j.1945-5100.2005.tb00149.x

Tornabene, L. L., Osinski, G. R., McEwen, A. S., Boyce, J. M., Bray, V. J., Caudill, C. M., et al. (2012). Widespread crater-related pitted materials on Mars: Further evidence for the role of target volatiles during the impact process. *Icarus*, *220*(2), 348–368. https://doi.org/10.1016/j.icarus.2012.05.022

Vaughan, W. M., Head, J. W., Wilson, L., & Hess, P. C. (2013). Geology and petrology of enormous volumes of impact melt on the Moon: A case study of the Orientale Basin impact melt sea. *Icarus*, *223*(2), 749–765. https://doi.org/10.1016/j.icarus.2013.01.017

Vincent, R. K. (1972). *An ERTS Multispectral Scanner Experiment for Mapping Iron Compounds*, *Vol. II, pp. 1239–1247* (). Ann Arbor, Michigan: Presented at the Proceedings of the Eighth International Symposium on Remote Sensing of Environment.

Viviano-Beck, C. E., Seelos, F. P., Murchie, S. L., Kahn, E. G., Seelos, K. D., Taylor, H. W., et al. (2014). Revised CRISM spectral parameters and summary products based on the currently detected mineral diversity on Mars. *Journal of Geophysical Research: Planets*, *119*, 1403–1431. https://doi.org/10.1002/2014JE004627

von Engelhardt, W. (1997). Suevite breccia of the Ries impact crater, Germany: Petrography, chemistry and shock metamorphism of crystalline rock clasts. *Meteoritics and Planetary Science*, *32*, 545–554. https://doi.org/10.1111/j.1945-5100.1997.tb01299.x

Young, K. E., van Soest, M. C., Hodges, K. V., Watson, E. B., Adams, B. A., & Lee, P. (2013). Impact thermochronology and the age of Haughton impact structure, Canada. *Geophysical Research Letters*, *40*, 3836–3840. https://doi.org/10.1002/grl.50745